remote sensing

Article

MeSat Mission: Exploring Martian Environment with THz Radiometer Payload and Optimal Trajectory

Vahid Rastinasab [1], Weidong Hu [1,*], Mohammadreza Saghamanesh [2], Kamel Djamel Eddine Kerrouche [3] and Mohammad Kazem Tahmasebi [4]

[1] School of Electronics and Information, Beijing Institute of Technology, Beijing 100811, China; 3820192078@bit.edu.cn
[2] Department of Engineering, Faculty of Space Engineering, Imam Hossein University, Tehran 16987-15461, Iran; msaghamanesh@ihu.ac.ir
[3] School of Automation Sciences and Electrical Engineering, Beihang University, Beijing 100191, China; kerrouche@buaa.edu.cn
[4] School of Mechanical Engineering, University of Science and Technology, Tehran 16846-13114, Iran
* Correspondence: hoowinf@bit.edu.cn; Tel.: +86-186-1239-7499

Abstract: Space exploration presents vast prospects for scientific, industrial, and economic progress. This paper introduces the MeSat mission as a pioneering approach to Mars exploration. The MeSat aims to deepen our understanding of Martian conditions and resources by employing an optimized Earth-to-Mars trajectory, enabling a comprehensive study of the Martian atmosphere and surface. The mission comprises a cargo microsatellite hosting three 6U CubeSats and two 3U CubeSats, deployed into four separate Mars orbits to form a constellation. Each CubeSat carries distinct payloads: a THz radiometer for Martian water vapor atmospheric observation, a high-resolution surface camera, a high-tech spectrometer, and a Fourier transform spectrometer (FTS) for wind speed readings. This paper includes the majority of the key parameters; however, we focus our discussion more on two aspects of this pioneering mission: the first aspect contains the proposal of four distinct payloads for the study of Mars' atmosphere and the second aspect proposes an optimal mission design algorithm that analyzes a fuel-efficient low-thrust trajectory from Earth to Mars. Regarding the payloads, the THz radiometer requires a specific design; hence, we explain this payload in more depth; the rest of the payloads, we suggest utilizing commercially available elements for the cost-effective manufacture of a whole system. For mission trajectory optimization, the study employs a dual-step hybrid optimization algorithm (PSO-homotopy) to analyze fuel-efficient low-thrust trajectories from Earth to Mars, incorporating the ephemeris dynamics model to account for gravitational perturbations in the entire Solar System. In practical mission design, crucial factors like hyperbolic excess velocity, diverse opportunities for Earth launch and Mars rendezvous, varied propulsion systems, and time of flight (TOF) play vital roles in trajectory optimization. In summary, for the MeSat mission, we propose a comprehensive Mars environmental mission design. We consider all aspects of the mission from trajectory design to engineering detail design, since we would like to inspire future Mars missions with a complete report.

Keywords: nanosatellite; CubeSat; THZ spectrometer; mars trajectory optimization; deep space exploration

Citation: Rastinasab, V.; Hu, W.; Saghamanesh, M.; Kerrouche, K.D.E.; Tahmasebi, M.K. MeSat Mission: Exploring Martian Environment with THz Radiometer Payload and Optimal Trajectory. *Remote Sens.* **2024**, *16*, 1893. https://doi.org/10.3390/rs16111893

Academic Editors: Siting Xiong, Yu Tao and Rui Song

Received: 6 March 2024
Revised: 15 April 2024
Accepted: 10 May 2024
Published: 24 May 2024

1. Introduction

Mars exploration, highlighted by NASA's plans for human missions by 2030, offers insights into exobiology, potential human settlement, and economic and scientific advancements, positioning Mars as a future second home for humanity and underscoring the importance of interplanetary missions [1–18]. Mars exploration began with NASA's Mariner 4 mission in 1964 [19]. The journey of Mars exploration continues with a host of landers, rovers, and orbiters to this day. In association with the Mars exploration missions, we also propose the exploration of Mars' environment through the introduction of MeSat orbiters. We focus on four distinct aspects of Martian scientific payloads for future missions, and propose an optimal trajectory for the orbit from Earth to Mars. The MeSat mission, equipped with four CubeSats carrying THz radiometers, FTS, cameras, and spectrometers, aims to form a constellation for Martian environmental analysis. Prior to embarking on the MeSat mission and to highlight how this scientific proposal contributes within existing Mars missions, we conducted a review of past Mars missions. Missions with scientific payloads such as Perseverance Rover [20] which sought ancient microbial life and introduced aerial exploration with Ingenuity. Tianwen-1 [21], China's comprehensive mission, examined Mars' geology and potential habitability. The Emirates' Hope Mission [22] focused on atmospheric and climate studies. InSight [23], alongside MarCO A and B, delved into Mars' deep interior. India's MOM [24] explored Mars with multiple payloads, including a methane sensor. NASA's Phoenix [25] and rovers Opportunity [26] and Spirit [27] analyzed soil and rock to uncover Mars' watery past and geological changes. Viking 1 and 2 orbiters monitored Martian weather, offering groundbreaking data on atmosphere composition and seasonal changes [28]. Mars Global Surveyor tracked atmospheric dust, temperature, and cloud movements, providing key insights into Martian weather systems [29]. Mars Odyssey used thermal emission imaging to study surface minerals and identify water ice [30].

Previous missions have primarily aimed at comprehending Mars' environmental characteristics, succinctly described as the pursuit to "know Mars better". Regarding previous missions and planned future Mars missions, we propose a MeSat mission (an expiration and inspiration scientific mission). The mission contains a THz radiometer for Martian atmospheric water vapor investigation, while wind velocity measurement using FTS payload, surface photography, and spectroscopic imaging are essential for outer space exploration.

For the measurement of water vapor, the following research and missions occurred. Between 1972 and 1974, the Mariner 9 mission utilized infrared spectroscopy to explore water vapor distribution in Mars' middle and upper atmosphere, developing a model extending up to 125 km [31]. Ideas in [32] claimed most of the water vapor was available in the 6 km–10 km region; those conclusions were proved using vertical water vapor analysis in the Viking 1 and 2 missions. Further research in [33] from thermal emission spectrometer (TES) data showed seasonal and hemispheric variations in Martian water vapor from March 1999 to March 2001. Differences were noted when compared to the Viking Orbiter findings. Furthermore, the Mars Climate Sounder (MCS) investigation was designed to measure the vertical resolution of the Mars atmosphere by understanding the Martian atmosphere water vapor with thermal emissions from the atmosphere [34]. The Mars Express mission presented a comprehensive five-Martian-year full seasonal water vapor investigation through vertical and longitudinal distribution [35]. Mars Express, equipped with IR spectrometer, operated in the 1.38 μm spectral bands [36]. The Compact Reconnaissance Imaging Spectrometer mission was expanded to acquire five Martian years of water vapor data above the North polar cap (NPC) [37]. Observation by planetary Fourier spectrometer long wavelength channel investigated day time water vapor abundance through the Martian atmosphere. This covered investigation through different latitudes, and different seasonal times [38]. Ice water particle research within the Martian atmosphere is presented within [39,40]. The examination of the vertical distribution of water vapor within 0–40 km of Mars' atmosphere was performed using infrared spectrometer; data processing showed cloud formation, ice water in the atmosphere, water vapor and subsurface water existence [41]. Monitoring the water vapor in the Martian atmosphere is crucial as it helps forecast weather, cloud formation, and thermal cycles, and identifies areas potentially rich in water vapor. Previous missions collected daytime data over several Martian years, enhancing our understanding of Mars' climate and identifying areas suitable for water existence and human colonization. The MeSat (the mothership) is equipped with an active THz radiometer to monitor the Martian atmosphere horizontally and deploys two 3U

CubeSats with passive THz radiometers for vertical monitoring. THz signals have high sensitivity to water vapor emissions [42]. By proposing this mission and monitoring Mars' atmosphere over several Martian years, the MeSat aims to provide comprehensive data on Martian water vapor distribution through both vertical and horizontal remote sensing, day and night. This complements existing water vapor data on the Martian atmosphere.

Measuring Martian wind speed is critical for understanding Mars' climate and atmospheric processes, as wind influences sediment transport, water vapor distribution, and thermal dynamics (this future mission is reported through the Mars Exploration Program Analysis Group) [43]. NASA's Viking 1 and 2 landers measured local wind speeds, and the Mars Express mission measured wind speed through the upper atmosphere. They were limited to their surroundings. The MeSat mission plans to deploy a 6U CubeSat equipped with an FTS payload that utilizes Doppler effects and is capable of measuring wind velocity on the Mars surface. This approach promises seasonal and global coverage, and a better understanding of Martian wind patterns to determine regional wind speed potentials for future human colonization and Mars climate impacts.

For the prospects of MeSat imaging and spectroscopy CubeSat, daily we see new cameras with better characteristics and resolution come in. There is always something new through which we can obtain high quality images of Mars [44].

The MeSat scenario involves launching a Cargo microsatellite from Earth to Mars. Four CubeSats will be transported by MeSat on this voyage to Mars' orbit. Once the Cargo reaches Mars, it dislodges four CubeSats to form the constellation that enables it to explore the Martian environment. The CubeSats communicate with the Cargo and transmit data to the mother ship and the mothership relays data to the Earth station. Figure 1 depicts the scenario.

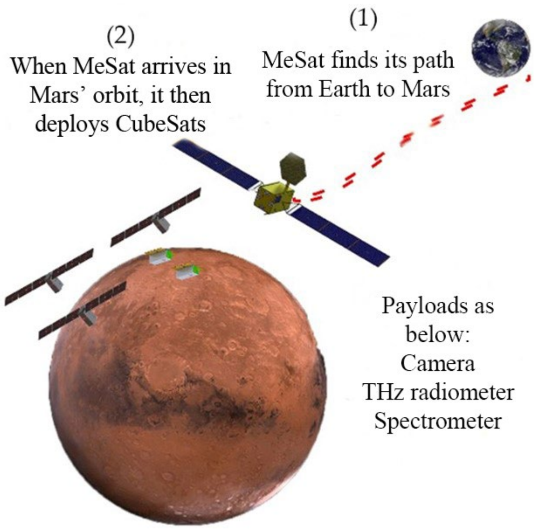

Figure 1. MeSat's scenario: (1) the microsatellite finds a path from Earth 's orbit to Mars; (2) when the microsatellite reaches Mars' orbit, it will deploy three 6U and two 3U CubeSats.

Each satellite in the proposed Mars mission is equipped with a distinct payload designed to gather data on the Martian surface and atmosphere. The instruments on CubeSats include a high-resolution camera, a HyperScape spectrometer with a range of 442–884 nm and a Fourier transform spectrometer (FTS) to enable measurement of Martian surface wind speed. To study the water vapor in Mars' atmosphere, we propose the usage of a THz radiometer. Water vapor in an exoplanet atmosphere is a major milestone on the way toward a habitable planet; water existence [45], cloud formation, thermal cycles [46], life signs [47] open a gate for finding other things [48].

We would like to propose a comprehensive mission within this report to inspire future space pioneering missions; therefore, we divided the main concepts of this paper into three main categories:

The first aspect of this study concerns the design of an optimal Earth-to-Mars mission, which involves identifying launch windows and minimizing fuel consumption while considering various factors and constraints [49]. A low-thrust trajectory mission from Earth to Mars is analyzed, taking into account gravitational perturbations due to all planets in the Solar System, solar-radiation pressure, and non-spherical perturbations of all planets. A PSO-homotopy dual-step hybrid optimization algorithm is employed to solve the resulting multipoint boundary value problems (MPBVP) accurately.

The second aspect of this study involves proposing four different sensors for a comprehensive study of Mars' environment and atmosphere. Each payload studies Mars from a different aspect. The camera is intended to capture photos of Mars' surface. The spectrometer can measure the approximate temperature of the surface and assist in future solar-cell establishment on the Mars surface. The FTS payload measures wind velocity and direction, assisting in the study of geological weather circulation in Mars' atmosphere and determining suitable locations for wind power plant construction and climate study on Mars. The THz payload is for water vapor detection in Mars' atmosphere, delivering a study on Martian atmospheric properties [50].

The third aspect of this study proposes an optimal system for satellites, which will be discussed in subsequent sections along with spacecrafts subsystem layouts, link budgets, mass budgets and satellite system budgets to support the proposed idea.

We present the MeSat mission as an inspiration for the future exploration of Mars' environmental boundaries. This multifaceted approach introduces novelty into Martian environmental research. The MeSat, presented as a proposal for future deep space exploration references, aims to inspire advancement in the field.

2. MeSat's Aims and Its Contrast with Previous Martian Projects

Over the last three decades, Mars exploration has received significant attention. In the following text, we analyze former Martian missions and at the end of this chapter, we show our contribution to future Martian space exploration missions.

The era commenced with the launch of the Mars Pathfinder mission in 1996 by NASA, which included the Sojourner rover. The Mars Pathfinder rover was outfitted with scientific instruments such as the alpha X-ray spectrometer, atmospheric/metrological instrument, three cameras for the Martian mission [51,52]. In 2001, NASA's Mars Odyssey mission embarked on a quest to search for evidence of water and ice beneath the Martian surface and aimed to provide communication relay for future Mars rovers [53]. The European Space Agency's Mars Express mission, launched in 2003, provided information about subsurface water on Mars, geological data, the atmosphere, and the history of water on Mars [54]. The deployment of NASA's twin rovers, Spirit and Opportunity, in 2003, marked an investigation into Mars' past weather and the history of its rivers; the twins' robots were equipped with spectrometer, camera, and rock grinder to analyze Mars' surface [55]. The Phoenix Mars Lander, launched in 2007, investigated the water–ice soil, and proposed additional instruments to investigate the planet's potential habitability. Phoenix consisted of a surface imager, gas analyzer, camera, microscopy, electrochemistry, and conductive analyzer [56]. In 2012, the Mars Science Laboratory mission delivered the Curiosity rover to Gale Crater, embarked on a journey to assess the habitability of Mars and study its climate and geology. Twenty-one cameras on the Curiosity rover platform covered diverse scientific missions, including photography cameras and a scientific spectrometer for Mars' surface discovery [57]. The MAVEN orbiter, initiated by NASA in 2014, began studying the upper layers of the Martian atmosphere, equipped with scientific instruments for monitoring solar wind, an electron analyzer, a solar wind ion analyzer, an extreme ultraviolet monitor, and a magnetometer [58]. The ExoMars Trace Gas Orbiter, a collaborative mission between the ESA and Roscosmos launched in 2016, focused on the analysis of trace gases such as methane to understand the active geological or biological processes on Mars and whether life ever existed on Mars or not [59]. NASA's InSight lander, launched in 2018, took Mars exploration below the surface, studying the planet's interior to unveil its seismic activity and internal heat flow. MarCo CubeSat, the first CubeSat mission to Mars, facilitated the InSight lander with data communication relay [60]. A new chapter in Mars exploration was written in 2020 with the launch of three missions: NASA's Mars 2020 with the Perseverance rover, aimed at collecting signs of life with scientific instruments, including a high quality spectrometry, weather station, and X-ray spectrometer [61]. CNSA's Tianwen-1, China's inaugural Mars mission, studied the Red Planet's morphology and geological characteristics, water–ice on the surface, climate and environment checks, and physical and internal environment checks [62]. The UAE's Hope Probe was designed to provide a comprehensive analysis of Mars' atmospheric data, an understanding of the dynamic weather and global weather mapping of Mars, and finding out how weather changes, and the break out of oxygen and hydrogen in the Martian atmosphere [63].

The aforementioned information presents an opportunity for the MeSat project. It is understood that previous missions have focused on the Martian atmospheric, environmental, meteorological, and internal body data, as well as water detection. These research endeavors have been accomplished to provide information on the possibility of transforming Mars into a habitable zone for humanity's second home. In light of previous research, it was observed that the majority of studies pertain to the Martian environment. Here, we aim to take a step further by investigating the Martian atmosphere and environment to propose appropriate locations for human colonization, identify the necessary conditions and suggest solutions.

To address that idea, we delineate several properties for MeSat. Firstly, we optimize the trajectory algorithm to minimize fuel consumption for the MeSat for an Earth to Mars orbit. Trajectory fuel optimization is a critical parameter for every outer space mission, as reduced power usage allows for increased payload mass, enabling the spacecraft to be equipped with additional instruments. Secondly, we propose deploying a CubeSat constellation into the Mars orbit, equipped with four individual sensors for investigating the Martian surface and atmosphere, to study suitable locations for future human habitation and enhance our understanding of the meteorology and climate of Mars. The Fourier transform spectrometer (FTS) payload measures wind velocity on the Martian surface and provides global Mars wind speed data. This information can identify areas with high potential for establishing wind turbines, capable of generating electricity for human habitats, cloud circulation and weather forecasting on Mars. The spectrometer payload assesses solar irradiance on the Martian surface, determining solar energy distribution and suggesting locations with optimal solar irradiation for the establishment of solar cells for electricity generation; additionally, we can send commands to measure other elements within spectrum ranges (442–884 nm). Complementing these payloads, a high-quality camera within another 6U CubeSat captures images of the Martian surface to identify flat areas suitable for human habitation and the associated construction requires better knowledge of Mars' surface. The combined data from the camera, spectrometer, and FTS payloads propose suitable locations for constructing human habitats with the capacity to utilize renewable energy for electricity generation. The THz radiometer payload is a scientific instrument for studying the Martian atmosphere and cloud formations, as THz frequency ranges have the potential to detect small particles of water vapor within the Martian atmosphere. This radiometer provides insights into cloud formation and thermal cycles within the Martian atmosphere.

The MeSat offers additional advantages. CubeSats are cost-effective, quickly assembled, and feature faster upgrade times and customization properties. For example, they can provide internet services in space, as well as photography, meteorology, and weather forecasting services. By altering the CubeSat payload with other types of payloads, we propose an optimized trajectory for the MeSat, hosting three 6U CubeSats and two 3U CubeSats, equivalent to approximately 24 kg. This mass can also accommodate other devices for a future human presence on Mars, such as a rover, lander, or scientific instruments.

The MeSat proposes multi-option missions to illustrate the capabilities of small satellites for space exploration and human colonization on extraterrestrial planets. The sensors proposed within the MeSat project offer prospective atmospheric and environmental investigations of Mars, aiming to inspire space exploration missions for the identification of humanity's second home in the near future.

3. MeSat: Mission Scenario and Technical Framework

The following sections consider the microsatellite expeditions from an earth-to-mars trajectory expansion to settle into the Mars orbit [64]. Figure 2 explains the expedition. Primarily, the MeSat enters Mars's orbit, and allocates orientation. In the next phase, the MeSat orbits the Mars axis to disgorge the CubeSats. Figure 3 depicts the CubeSat modes. All single modes are then reconnoitered.

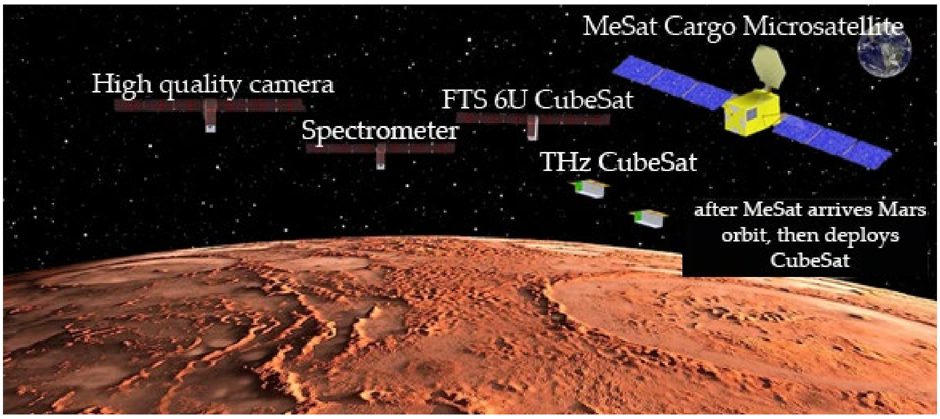

Figure 2. MeSat operational outlook in orbit of Mars.

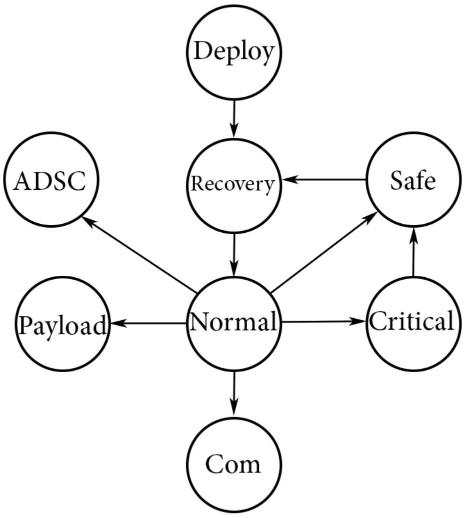

Figure 3. CubeSat modes description.

Safe mode: Safe mode is initiated after the CubeSats are deployed from the MeSat into Mars' orbit. In this mode, the CubeSats power up their electronic power subsystem (EPS) and on-board data handling subsystem (OBDH). They then wait for 15 min to ensure that their batteries are charged, and deployable mechanisms are properly ready. Once this is achieved, the CubeSats broadcast beacon signals to indicate their presence and undertake the next mode of operation. The safe mode is critical for the CubeSats' successful deployment and operation in the Martian environment.

Recovery mode: The recovery mode involves the CubeSat's attitude determination and control subsystem (ADCS) adjusting the orientation of the CubeSats to a nadir pointing attitude, which is necessary for the payloads on the CubeSats to operate effectively on the Martian surface. Once the CubeSats are oriented correctly, they broadcast a beacon signal to indicate their readiness and enter normal mode. This mode enables the CubeSats to perform their primary scientific objectives on the Martian surface.

Normal mode: The CubeSats are put in standby mode and await commands from the ground segment. The ground segment can direct the CubeSats to perform various functions such as in ADCS, communication, or payload mode. The microsatellite acts as a relay between the CubeSats and the Deep Space Network (DSN) in all modes.

Payload mode: In payload mode, the CubeSat activates the scientific instruments onboard to collect data about Mars. This could include information about the planet's atmosphere, surface, or any other scientific measurements the CubeSat was designed to make. The data is then stored on a secure digital (SD) card. Once the SD card is full, the CubeSat automatically switches to communication mode to transmit the data back to Earth. This is an important step in the mission, as the scientific data collected by the CubeSats can provide valuable information for research and exploration purposes.

Communication mode: In communication mode, new commands received from ground segment directives (GSD) are executed. These commands can either be directed to the microsatellite to broadcast to the CubeSats, or to one of the CubeSats to transmit payload data back to the microsatellite for relay to GSD. If any anomalies occur during operation, the CubeSats can jump to Safe mode, where all subsystems turn OFF and the batteries recharge to increase power levels. After executing each functional mode, the CubeSats return to normal mode and wait for new GS commands.

Attitude determination and control system (ADCS) mode: This mode follows the safe mode operation. During safe mode, all satellite subsystems are deactivated, and there is a high probability that the satellites deviate from their primary orientation towards the Mars nadir point. The attitude determination and control system (ADCS) mode is subsequently engaged to re-adjust the satellite orientation to the correct direction. This correction can be based on a ground command or a preprogrammed orientation.

Critical mode: Critical mode refers to an emergency status when satellite power level is below 20%, then the satellite enters this critical mode, shuts down all subsystems and the main computer enters sleep mode. Once the battery power level rises above 80%, the satellite enters normal mode.

3.1. CubeSat Power Subsystem Performance and Functions Methodology

In this proposed 6U nanosatellite platform, each wing is composed of three solar panels, as shown in Figure 4, where each wing has a power of up to 45 W (in STC conditions) and is made up of 5S + 5S + 5S solar cells on each panel.

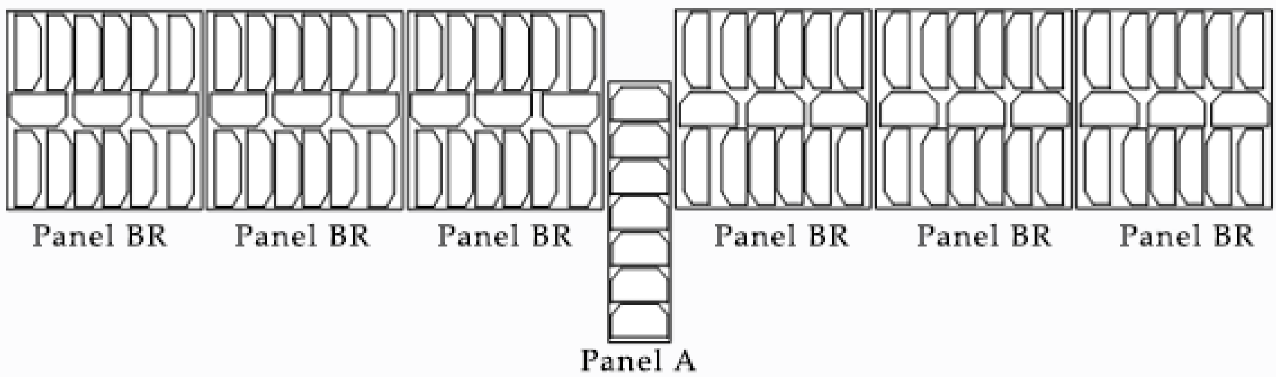

Figure 4. Configuration of 6U CubeSat solar panels.

The parameters of solar panel A with seven cells are presented in Table 1:

Table 1. Solar panel "A" electrical parameters BOL and EOL at 28 °C.

Parameter	BOL	EOL		
Fluence @ 1MeV [e/sq cm]	0	2.50×10^{14}	5.00×10^{14}	1.00×10^{15}
Estimated Pmp	1.00	0.97	0.94	0.90
Voc [V]	18.83	18.24	17.88	17.58
Isc [A]	0.52	0.52	0.51	0.50
Vmp [V]	16.86	16.40	16.02	15.71
Imp [A]	0.5	0.502	0.499	0.485
Pmp [W]	8.48	8.23	7.99	7.62

On Mars, the solar irradiance is 586.2 W/m^2, very low compared to that obtained in Earth's orbits. Therefore, the solar panel power estimation is shown in Table 2:

Table 2. 6U CubeSats Solar panel power estimation.

Solar Panel Type	Estimation of Power (W)
Solar panel A	3.6
Solar panel BR	7.4
Total solar panels	48

In this proposed project, two 3U THz nanosatellites are used to perform the mission. In the primary source of the power system, as shown in Figure 5, three panels generate power and each panel is composed of seven solar cells, with each solar panel producing power of up to 8.48 W (STC).

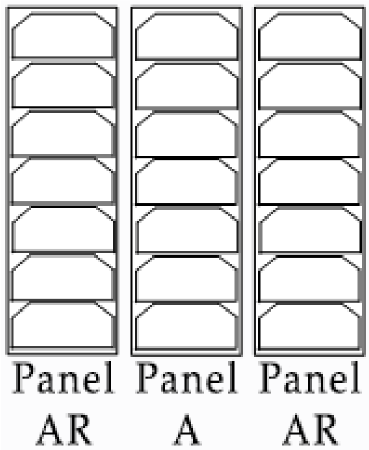

Figure 5. Configuration of 3U CubeSat solar panels.

In comparison to the solar irradiance obtained in Earth's orbit, the solar irradiance on Mars is quite low, achieving 586.2 W/m^2. Table 3 depicts the estimated power of the solar panels.

Table 3. 3U CubeSat Solar panel power estimation.

Solar Panel Type	Estimation of Power (W)
Solar panel A	3.6
Solar panel AR/AL	3.6
Total solar panels	10.8

To validate the power system and layout of the solar cells on the satellite, we conducted an investigation into the CubeSat's power budget, as outlined in Tables 4–7.

Table 4. FTS 6U CubeSat power budget estimation in Mars orbit.

Modes	Active Subsystems	Power Usage (W)
Recovery	MCU, EPS, star tracker, thruster	21.6
Normal	MCU, EPS, TTC RX	1.140
ADCS	MCU, thruster, star tracker, EPS, reaction wheels	29.6
Payload	FTS, MCU, EPS, reaction wheels, star tracker	29
Com	MCU, EPS, TX	6
Critical	MCU (LOW power), EPS	0.5
Safe	MCU, EPS	0.9
Peak power usage		29.6
Margin		18.4

Table 5. High quality camera 6U CubeSat power budget estimation in Mars orbit.

Modes	Active Subsystems	Power Usage (W)
Recovery	MCU, EPS, star tracker, thruster	21.6
Normal	MCU, EPS, TTC RX	1.140
ADCS	MCU, thruster, star tracker, EPS, reaction wheels	29.6
Payload	Camera, MCU, EPS, reaction wheels, star tracker	18.5
Com	MCU, EPS, TX	6
Critical	MCU (LOW power), EPS	0.5
Safe	MCU, EPS	0.9
Peak power usage		29.6
Margin		18.4

Table 6. HyperScape 100 spectrometer 6U CubeSat power budget estimation in Mars orbit.

Modes	Active Subsystems	Power Usage (W)
Recovery	MCU, EPS, star tracker, thruster	21.6
Normal	MCU, EPS, TTC RX	1.140
ADCS	MCU, thruster, star tracker, EPS, reaction wheels	29.6
Payload	Spectrometer, MCU, EPS, reaction wheels, star tracker	14.8
Com	MCU, EPS, TX	6
Critical	MCU(LOW power),EPS	0.5
Safe	MCU, EPS	0.9
Peak power usage		29.6
Margin		18.4

Table 7. THz payload 3U CubeSat power budget estimation in Mars orbit.

Modes	Active Subsystems	Power Usage (W)
Safe	OBDH, ADCS, MCU, ADCS sensors	1.616
Recovery	OBDH, ADCS, MCU, ADCS sensors, thruster	2
Normal	OBDH, ADCS, MCU, ADCS sensors, UHF RX/TX	2.16
Communication	OBDH, ADCS, MCU, ADCS sensors, S-band, thruster	2.276
Payload	OBDH, ADCS, MCU, ADCS sensors, THz	5
Peak power usage		5
Margin		3

3.2. Link Budget

In order to ensure reliable communication between the cargo microsatellite and the Deep Space Network (DSN), a link budget analysis must be performed. This analysis takes into account various factors such as the transmit power of the microsatellite, the antenna gain, the distance between the microsatellite and the DSN, and the noise figure of the receiving system. By calculating the link budget, we can determine the expected signal strength at the DSN receiver and ensure that it is above the minimum threshold required for reliable communication [65]. This is critical for the success of the mission, as the cargo microsatellite serves as the primary means of relaying data between the mothership and the CubeSats. Refer to Table 8 for the link budget calculations between the mothership and the Deep Space Network (DSN). As the mothership is responsible for directly relaying data to the ground-based DSN, it is crucial to evaluate the link budget between these two nodes [66].

Table 8. Mothership to DSN link budget calculation.

Future	Quantity
Total transmitter power	38.45 dBm
Transmitter circuit losses	−0.25 dB
MarVen antenna gain	29.2 dBi
Antenna pointing loss	−0.1 dB
EIRP	67.3 dBm
Path loss (Mars to Earth)	−279.33 dB
Atmospheric attenuation	−0.14 dB
DSN parameter	
Polarization losses	−0.3 dB
Antenna pointing loss	−0.3 dB
DSN (DSS 14) antenna gain	74.28 dB
DSN circuit loss	−1.79
SNT (system noise temperature)	18.39 K
SNT due to elevation	5.023 K
SNT due to atmospheric	8.6 K
SNT due to Sun	0.00 K
SNT due to hot body	0.00 K
Total system noise temperature	32.01 K
Noise spectral density	−183.55 dBm/Hz
E_b/N_0	43.19 dB-Hz
Threshold E_b/N_0	38.3 dB-Hz
Margin	4.89

4. Mission Design Analysis for Low-Thrust Trajectory Optimization to Mars Considering Full Perturbation System

In practical mission design analysis, various factors play crucial roles and impose constraints on trajectory planning. Hyperbolic excess velocity, launch and rendezvous dates, thruster types, time of flight (TOF), and the optimization methodology are among the pivotal considerations. Additionally, technological limitations, such as spacecraft thruster specifications or subsystem constraints, introduce further constraints which shape the mission parameters. This practical approach, considering diverse constraints, adds realism to mission design analysis in real-world scenarios.

These ephemeris perturbations have the potential to significantly alter optimal spacecraft trajectories. This study specifically focuses on analyzing fuel-optimal low-thrust trajectories from Earth to Mars while incorporating the ephemeris model. Handling the resulting two-point boundary value problem (TPBVP) becomes notably more challenging compared to a simplified 2B dynamical model.

To address this complexity, the study demonstrates the application of a dual-step hybrid optimization algorithm (PSO-homotopy). This algorithm facilitates the solution of the resulting multipoint boundary value problem (MPBVP) with remarkable accuracy, effectively meeting the specified constraints.

Furthermore, the research investigates the effects of hyperbolic excess velocity, diverse Earth launch and Mars rendezvous opportunities, as well as different propulsion systems like Hall thrusters and Ion engines. Notably, the findings reveal the feasibility of delivering a 102.8 kg payload to Mars while consuming a mere 17.2 kg of fuel, highlighting the efficiency and optimization achieved in the trajectory planning.

4.1. System Description

In an ephemeris model, it is essential to take into account perturbing accelerations resulting from: (1) $\mathcal{F}_s$: solar radiation pressure, (2) $\mathcal{F}_{J2}$: oblateness impacts of celestial bodies, and (3) $\mathcal{F}_p$: other celestial bodies of the Solar System. The disturbing accelerations are conceptualized as [66]

$$\begin{array}{l} \mathcal{F}_p = -\frac{\mu_{pl}}{\|r-r_{pl}\|^3}\left(r - r_{pl}\right) - \frac{\mu_{pl}}{\|r_{pl}\|^3} r_{pl}, \\ \mathcal{F}_{J2.} = -\frac{\mu_{pl} r_0^2 J_2}{2r^5}\left(3r + 6r\sin\varphi \frac{\partial z}{\partial r} - 15r\sin^2\varphi\right), \\ \mathcal{F}_s = \beta \frac{r}{mr^3}\ ;\ \beta = \frac{\sigma^*}{\sigma}. \end{array} \tag{1}$$

where r_{pl} and μ_{pl} show the position vector and the gravitational constant of a planet, $\partial z/\partial r = [0\ 0\ 1]^T$, φ represents the planet-centric latitude, σ is a constant flight loading ($\sigma = m/A$ where A is the unit area), σ^* is determined as 1.53 (gm^{-2}), β and r signify the solar radiation pressure and the spacecraft position vector, in the heliocentric equatorial reference frame (HERF). The dynamics system is modeled as follows [67]:

$$\dot{x} = \begin{cases} \dot{r} = v, \\ \dot{v} = -\dfrac{\mu}{r^3} r + \dfrac{T_{\max} u}{m}\alpha + \sum \mathcal{F}_p + \sum \mathcal{F}_{J2.} + \mathcal{F}_s, \\ \dot{m} = -\dfrac{T_{\max}}{c} u, \end{cases} \tag{2}$$

Here, m and $v \in \mathbb{R}^3$ represent the updated spacecraft mass and the spacecraft velocity vector, respectively. The spacecraft's propulsion vector is modeled as $T = uT_{max}\alpha$, where $T_{\max}$ is the maximum thrust magnitude, $u \in [0,\ 1]$ represents the engine throttle magnitude, and α the unit thrust steering vector. The constant $c = I_{\mathrm{sp}} g_0$ denotes the effective exhaust velocity of the propulsion system. Here, g_0 denotes the Earth's sea-level gravitational acceleration, μ denotes the Sun's gravitational parameter, and I_{sp} denotes the thruster-specific impulse.

4.2. Low-Thrust Trajectory Optimization Description

The performance index of a fuel-optimal trajectory is represented by J_a as an auxiliary homotopy performance index [68]

$$J = \int_{t_0}^{t_f} \frac{T_{\max}}{c} u\, dt \Rightarrow J_a = \lambda_0 \int_{t_0}^{t_f} \frac{T_{\max}}{c} [u - \varepsilon u(1-u)]\, dt. \tag{3}$$

Here, $\lambda_0 \in (0,1]$ denotes a constant auxiliary multiplier, ε denotes a continuation parameter, where $\varepsilon = 1$ and $\varepsilon = 0$ correspond to the energy-optimal and fuel-optimal problems. These developments are deployed with dual objectives: (1) mitigating the challenges linked to the inherent bang-bang control problem in fuel-optimal solutions using a homotopic method; (2) leveraging the homogeneity of the resulting equation set to effectively constrain the search space. Consider $\lambda = \left[\lambda_0, \lambda_r^T,\ \lambda_v^T,\ \lambda_m\right]^T$ as the vector of co-states. It is worth noting that λ_0 represents one of the unknown parameters, remaining constant throughout the homotopic algorithm. The application of Pontryagin's minimum principle, in conjunction with primer vector theory, results in the following extremal controls [69]:

$$\alpha = -\frac{\lambda_v}{\|\lambda_v\|}\ ,\ u = \begin{cases} 0 & \rho > \varepsilon \\ 1 & \rho < -\varepsilon \\ \frac{1}{2} - \frac{\rho}{2\varepsilon} & |\rho| \leq \varepsilon \end{cases},\ \rho = 1 - \frac{c\|\lambda_v\|}{m\lambda_0} - \frac{\lambda_m}{\lambda_0}. \tag{4}$$

Here, ρ represents the switching function. The co-state dynamics, given by $\dot{\lambda} = -[\partial H/\partial x]^T$, are derived through Euler–Lagrange conditions. Consequently, the set of state/co-state dynamics become:

$$\begin{cases} \dot{r} = v, \\ \dot{v} = -\frac{\mu}{r^3}r + \frac{T_{\max}u}{m}\alpha + \sum\mathcal{F}_p + \sum\mathcal{F}_{J2.} + \mathcal{F}_s, \\ \dot{m} = -\frac{T_{\max}}{c}u, \\ \dot{\lambda}_r = \frac{\mu}{r^3}\lambda_v - \frac{3\mu\lambda_v.\,r}{r^5}r - \sum\left(\frac{3\mu_{Pl}\lambda_v.(r-r_{Pl})}{\|r-r_{Pl}\|^5}(r-r_{Pl}) - \frac{\mu_{Pl}\lambda_v}{\|r-r_{Pl}\|^3}\right) - \beta\left(\frac{\lambda_v}{mr^3} - \frac{3\lambda_v.\,r}{r^5}r\right) \\ \quad -\sum\left[\frac{15\mu_{Pl}r_0^2J_2}{2}\left(\frac{\sin^2\varphi}{r^5}\lambda_v - \frac{7\sin^2\varphi(\lambda_v.\,r)}{r^7}r + \frac{2\sin\varphi(\lambda_v.\,r)}{r^6}\frac{\partial z}{\partial r}\right)\right. \\ \quad \left. -\frac{\mu_{Pl}r_0^2J_2}{2}\left(\frac{3\lambda_v}{r^5} - \frac{15(\lambda_v.\,r)}{r^7}r\right) - 3\mu_{Pl}r_0^2J_2\left(\lambda_v.\frac{\partial z}{\partial r}\right)\left(-\frac{5\sin\varphi}{r^6}r + \frac{1}{r^5}\frac{\partial z}{\partial r}\right)\right], \\ \dot{\lambda}_v = -\lambda_r, \\ \dot{\lambda}_m = -\frac{T_{\max}u}{m^2}\|\lambda_v\| - \beta\frac{\lambda_v.\,r}{m^2r^3}. \end{cases} \tag{5}$$

4.3. Numerical Simulations

This study focuses on analyzing fuel-optimal low-thrust trajectories for missions from Earth to Mars, considering ephemeris perturbations. The research demonstrates the application of a dual-step hybrid optimization algorithm (PSO-homotopy) to solve the resulting multipoint boundary value problem (MPBVP) with high accuracy in satisfying the various constraints.

Moreover, the impact of different factors such as hyperbolic excess velocity, various Earth launch and Mars rendezvous opportunities, and various types of propulsion systems like Hall thrusters and Ion engines are investigated. The analysis aims to determine their effects on the mission's outcome.

The research explores scenarios where the hyperbolic excess velocity $\left(v_{\infty_i}\right)$ ranges between -2 (km/s) and 2 (km/s). Furthermore, the study considers variations in initial and final conditions, final date t_f, initial date t_0, and time of flight (TOF). The Earth launch and Mars rendezvous windows are set within the timeframe of [1 January 2024, 31 December 2026], where 1 January 2024 marks the start date of the search and 31 December 2026 serves as the final date.

TOF, calculated as the difference between t_f and t_0, significantly influences the positioning and velocity of Mars at the end of the flight. The initial states of the Earth also rely on t_0. The heliocentric position and velocity data for both Earth and Mars are sourced from the JPL/HORIZONS database, providing accurate planetary information for analysis and computations.

The analysis is conducted on thirty available thrusters, as detailed in Table 9, aiming to identify the most effective thruster considering a new thrust modeling approach. The assessment leads to the determination that the RIT-22 Ion engine stands out as the most suitable thruster for this particular scenario. The RIT-22 Ion engine exhibits remarkable performance characteristics with a maximum thrust of $T_{\max} = 250(\text{mN})$, specific impulse of $I_{\text{sp}} = 6400(\text{s})$, and a mass of 7 kg.

Table 9. Specifications of the thrusters considered in the solution.

Name, Ref. [70]	$T_{\mathbf{max}}$ (mN)	m_e (kg)	$I_{\mathbf{sp}}$ (s)	$P_{\mathbf{max}}$ (kW)	η (%)
Ion Engines					
NSTAR	92.7	8.20	2500	2.325	61.8
DERA T6	150.0	6.20	3470	3.900	65.0
25 cm XIPS Hughes	165.0	NA	3500	4.500	65.0
NASA 30 cm	178.0	7.00	3610	4.880	67.0
RIT-XT	210.0	NA	4448	6.850	75.5
NEXT	238.0	12.7	4070	6.860	59.0
RIT-22	250.0	7.00	6400	5.0	NA
HiPER DS3G	450.0	NA	10,000	25.0	NA
NEXIS	470.0	28.70	8500	25.0	78.0
Prior Thruster	500.0	20.0	2000	NA	NA
HiPEP	**670.0**	**46.50**	**9620**	**39.300**	**80.0**
Hall-Effect Thrusters					
BHT-1500	102.0	NA	1820	1.7	54.6
Thales HEMP	152.0	6.0	3500	3.0	58.0
P5	246.0	NA	2326	5.0	NA
DS-HET	300.0	12.0	3000	5.0	50.0
SPT-140	300.0	NA	1750	5.0	55.0
T-140	300.0	NA	2000	4.5	NA
PPSX000	340.0	NA	2480	6.0	NA
NASA-137Mv2	342.0	NA	3000	7.872	59.6
SPT-160	400.0	NA	2500	4.5	60.0
SPT-200	498.0	NA	2250	11.0	63.0
BHT-8000	512.0	20.0	1900	8.0	60.0
T-220	1000.0	NA	1950	20.0	62.0
PPS-20k ML	1050.0	25.0	2500	22.4	60.0
SPT-290	1500.0	23.0	3300	30.0	70.0

Based on these findings, reflected in Table 10, the optimization process resulted in an optimal spacecraft final mass of $m_f = 102.8$ (kg). Additionally, the optimization procedure determined the following key mission parameters:

Optimal hyperbolic excess velocity: $v_\infty = -0.5$ (km/s)
Launch date: $t_0 = 10$ April 2024
Mars rendezvous date: $t_f = 24$ March 2025
Time of flight (TOF): 348 days

Table 10. Parameters and optimal boundary values for Earth–Mars mission.

Parameter	Optimal Solution
Initial time, t_0 (TDB; JD)	10 April 2024; 2460410.5
Time of flight (days)	348
Final time, t_f (TDB; JD)	24 March 2025; 52460758.5
$r_E(t_0)$ (km)	$[-1.41697171828695 \times 10^8, -5.24872600577300 \times 10^7, 3.41954334262199 \times 10^4]$
$v_E(t_0)$ (km/s)	$[9.858836758211465 \times 10^0, -2.807567589144283 \times 10^1, 2.475556862844286 \times 10^{-4}]$
$r_M\left(t_f\right)$ (km)	$[-2.062255095916851 \times 10^8\ 1.393403861898105 \times 10^8, 7.999954257281169 \times 10^6]$
$v_M\left(t_f\right)$ (km/s)	$[-1.27286229760030 \times 10^1, -1.795386400481246 \times 10^1, -6.391620818469512 \times 10^{-2}]$
m_0 (kg)	120
I_{sp} (s)	6400
T_{max} (mN)	250

This optimized configuration represents the most efficient combination of spacecraft characteristics and mission timing to achieve the delivery of a 102.8 kg payload to Mars using the RIT-22 Ion engine while adhering to the specified hyperbolic excess velocity and mission timelines.

Figure 6 displays the time evolution of planetary gravity perturbations along the trajectory with a hyperbolic excess velocity of $v_\infty = -0.5$ (km/s). This figure illustrates how the influence of Mars' gravity potential gradually increases over time, becoming significant as the spacecraft enters Mars' sphere of influence (SOI). Additionally, it showcases the impact of solar radiation pressure perturbations on the spacecraft's trajectory, considering the instantaneous spacecraft mass. Furthermore, Figure 6 depicts the perturbing acceleration due to the second zonal harmonic (J_2) for Earth, with noticeable effects observed within Earth's SOI, especially when the spacecraft approaches Earth.

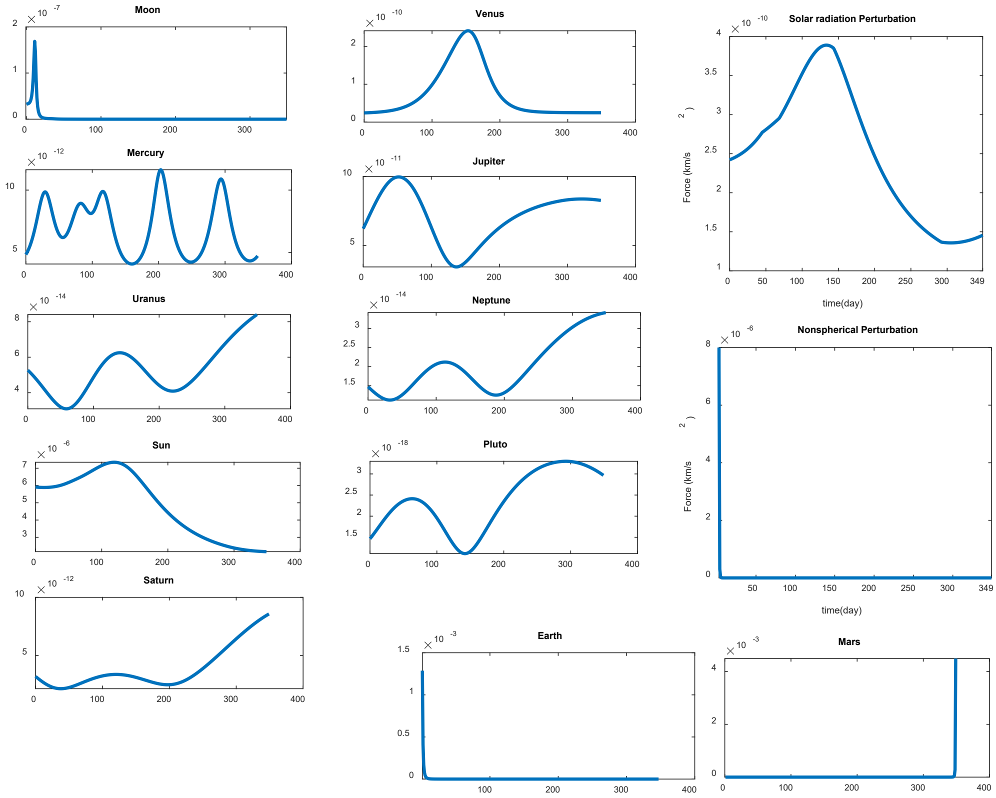

Figure 6. Time history of magnitude of perturbations.

The attractiveness of this analytical tool lies in its capability to provide high-resolution and accurate solutions. This is achieved through the utilization of a hybrid optimization method in formulating and solving the resulting optimal control problems (OCPs).

Figure 7 presents the energy-optimal and fuel-optimal thrust profiles specifically tailored for the RIT-22 Ion engine. Moreover, Figures 8 and 9 showcase the fuel-optimal bang-bang control trajectory based on the ephemeris dynamical model with a comprehensive perturbation system. The differences in mass between energy-optimal and fuel-optimal solutions for this dynamical model are visually depicted in Figures 10 and 11.

Furthermore, Figure 12 illustrates the influence of the dynamical model on the time evolution of the elements within the co-state vector, where the co-states are restricted within the domain of $[-1, 1]$. Remarkably, the shooting function accuracy errors of the fuel-optimal solution demonstrate small values, with final condition errors reported as $\Delta r_f = 5 \times 10^{-6}(\mathrm{km})$ and $\Delta v_f = 1.5 \times 10^{-11}(\mathrm{km/s})$.

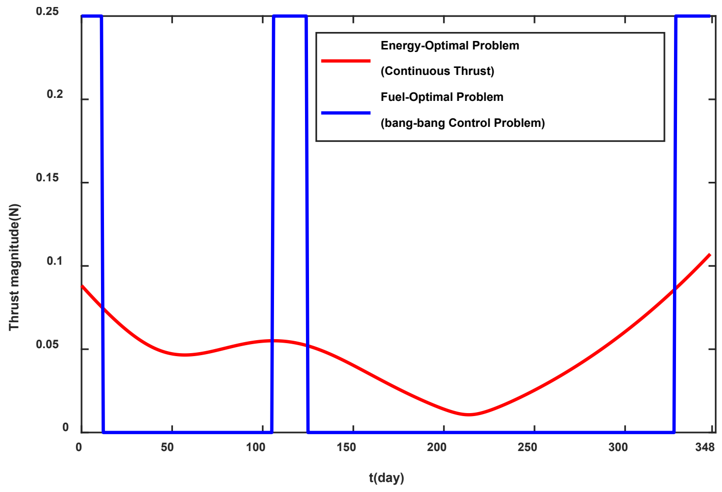

Figure 7. Comparison of energy- and fuel-optimal thrust profiles.

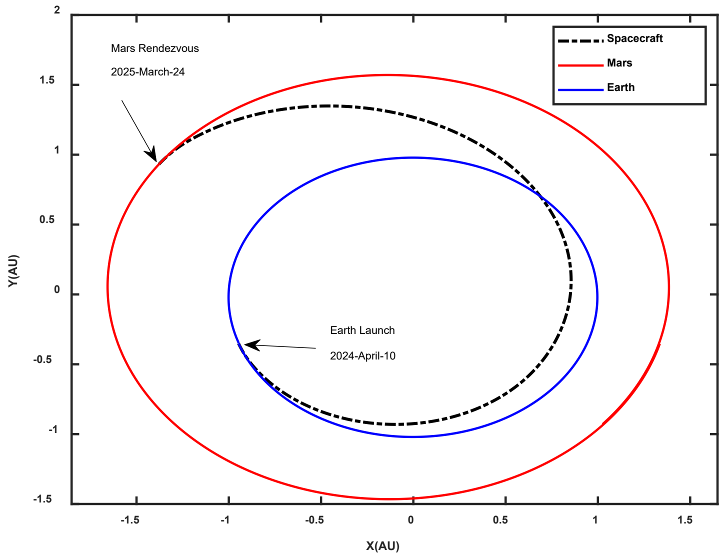

Figure 8. Two-dimensional fuel-optimal trajectory.

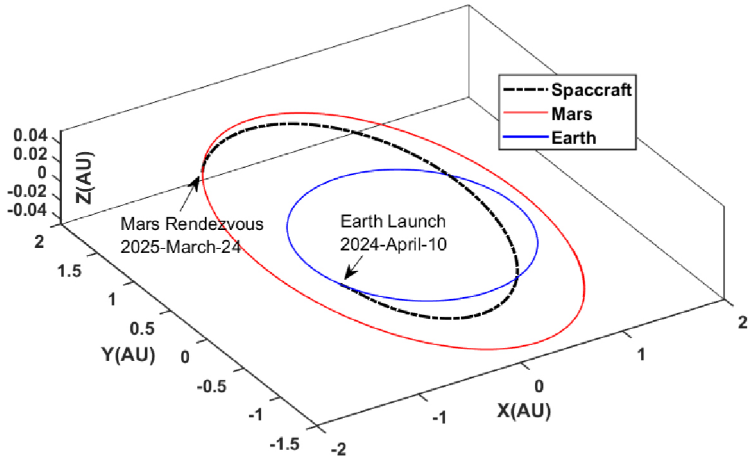

Figure 9. Three-dimensional fuel-optimal trajectory.

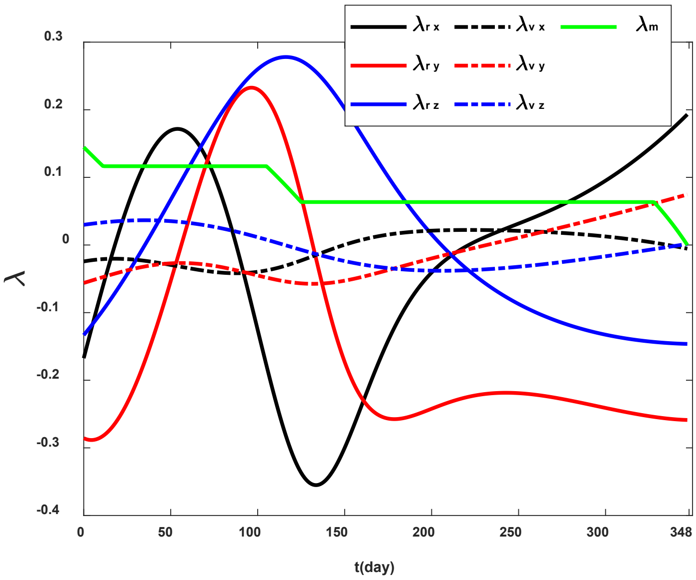

Figure 10. Comparison of fuel-optimal co-state vectors.

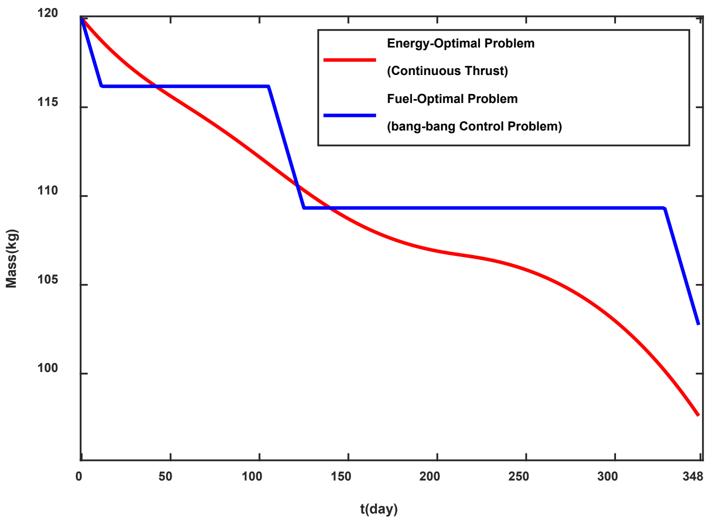

Figure 11. Comparison of optimal masses $m\left(t_f, \varepsilon\right)$ for energy- and fuel-optimal profiles.

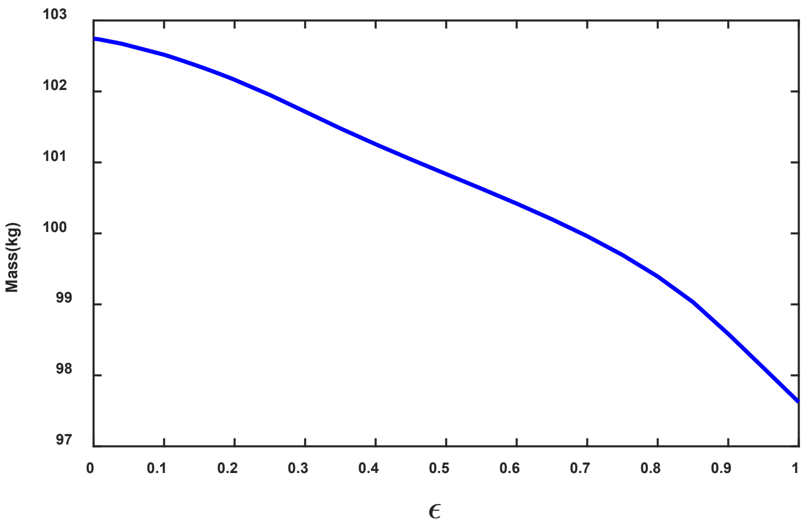

Figure 12. Comparison of energy-optimal trajectory to fuel-optimal trajectory.

Despite achieving a high level of accuracy in the optimal solution, the terminal mass of the proposed solution has been increased to 102.8 kg. This augmentation is a result of employing various efficient optimization techniques, such as adjusting the hyperbolic excess velocity, exploring different Earth launch and Mars rendezvous opportunities, evaluating different types of thrusters, optimizing the time of flight (TOF), and leveraging the hybrid optimization method. These strategies collectively contribute to refining the solution towards the specified objectives.

5. MeSat Mission Satellite System Design

The MeSat mission is composed of five satellites, including one mothership, two 3U CubeSats, and three 6U CubeSats, all integral to the comprehensive investigation of Mars' environment. Each satellite plays a crucial role in the mission, requiring accurate design considerations for various aspects, including power systems, communication protocols, mass distribution, and subsystem layouts. In this phase, we design the subsystems of the satellites.

5.1. Cargo Microsatellite

The cargo microsatellite serves as an effective satellite in the MeSat initiative. Its primary function is to carry the CubeSats from Earth to Mars, facilitating their exploratory endeavors on the Martian terrain. The specifications of the microsatellite are depicted in Figure 13, which reveal that it has a total mass of 120 kg and occupies dimensions of 60 × 60 × 100 cm; see Table 11 for the mass budget for the cargo microsatellite.

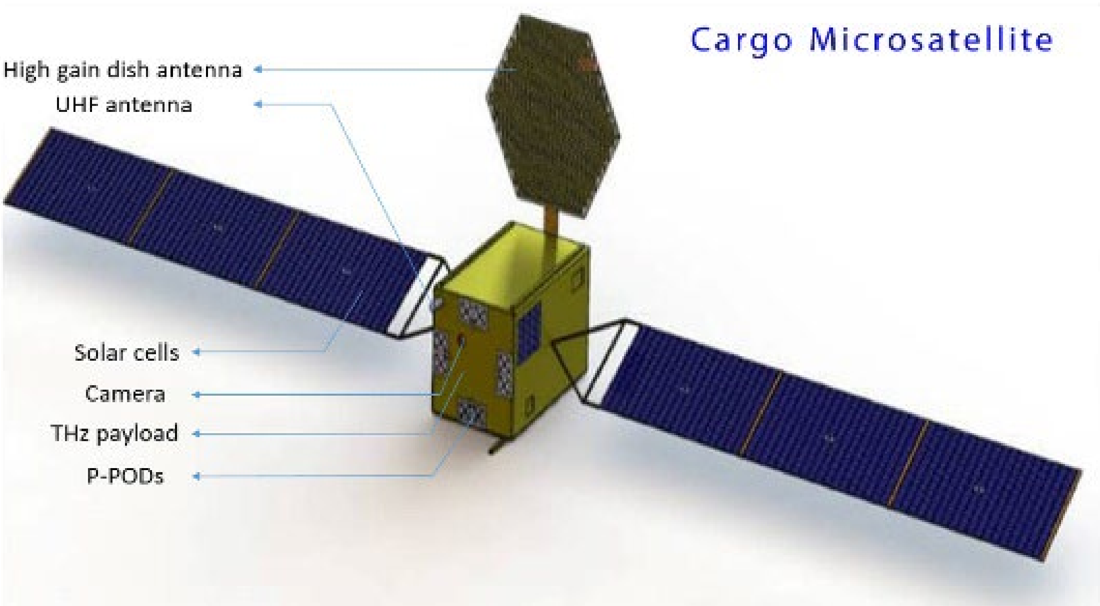

Figure 13. The cargo microsatellite specifications.

Telemetry tracking and command system: For direct communication with the Deep Space Network (DSN), the cargo microsatellite utilizes a high gain reflect array X-band antenna. The downlink data is transmitted via an X-band transmitter with a selectable bitrate, capable of achieving a maximum data rate of 100 Mbps with QPSK/OQPSK modulation. This transmitter enables the transmission of data directly to Earth. In addition, a UHF transceiver is utilized for data communication between the mothership and the CubeSats.

On-board data handling: Two microcontrollers are employed in the cargo microsatellite for command and data handling purposes. The Aeroflex GR712 computer board is responsible for managing the trajectory and attitude control algorithm. On the other hand, an STM32-based microcontroller is utilized to supervise the rest of the subsystems such as telemetry, tracking and command (TTC), electrical power system (EPS), payload, and ultra-high frequency (UHF) communication. The utilization of two microcontrollers in the cargo microsatellite provides enhanced control over the spacecraft's various subsystems, ensuring smooth and efficient operations.

Table 11. Cargo microsatellite mass budget.

Subsystem	Quantity	Mass (gr)
	TTC	
X-band	1	3000
UHF-band	1	75
	OBDH	
MCU 1Aeroflex GR712 ADCS	1	94
MCU 2	1	196
	Payload	
THz radiometer	1	1000
Camera	1	250
6U CubeSat	3	6U CubeSat with FTS payload = 8951 6U CubeSat with HyperScape spectrometer payload = 6664 6U CubeSat with camera payload = 6664
3U CubeSat	2	3U CubeSat with THz payload = 2qtyx2761
P-PODs	3x6U 2x3U	3 × 12,000
	EPS	
6U solar cells	8	8 × 300
Batteries and hardware	1	722
	ADCS	
Reaction wheels, IMU sensors	1	6000
DARE T6 Ion thruster	1	7000
Fuel back capacity		17,000
Reserved fuel for pioneering missions		7000
	STR and TCS	
Structure		10,000
Thermal control		4350
Total		120,000

Payload: The cargo is equipped with several essential instruments such as a high-resolution camera, a THz receiver, and Poly Picosatellite Orbital Deployers (P-PODs). The camera captures images during the ejection of the CubeSats, and these images are transmitted to the DSN for verification of the CubeSats' deployment. The THz receiver is an important tool that will be used to specify water vapor in the Martian atmosphere. Additionally, the P-PODs are utilized to release the CubeSats into space. The successful deployment of these CubeSats will be a critical step towards achieving the mission objectives.

Electrical power system (EPS): The EPS system of the cargo is equipped with eight sets of 6U solar cells that provide power to the electrical subsystems. In addition, a 100 Wh battery power generator is included to support the system during periods of low solar energy, such as when the spacecraft is in shadow or during periods of high-power consumption.

Attitude determination and control system: The cargo microsatellite uses DARE T6 Ion thruster to transport the CubeSats from Earth to Mars. Reaction wheels and Star tracker are subsequently used for attitude control and determination on Mars.

5.2. CubeSats System Design

MeSat facilitates identification of Martian features through the deployment of five distinct CubeSats. Each mission within the MeSat project is dedicated to the precise identification of specific environmental characteristics on Mars. The following elucidates the features and objectives of each CubeSat system within the project.

The 6U CubeSat with FTS payload: The Fourier transform spectrometer (FTS) is an important payload for measuring wind velocities from space with high accuracy. This payload can be integrated into a 6U CubeSat. In this case, it is specifically designed for observing the wind spectrum on Mars. The payload specifications are listed in Table 12. The FTS payload consists of an interferometer with a spectral resolution of 0.05 cm^{-1} and a spectral range of 1–12 microns. It is equipped with a linear array detector with a pixel size of 17 × 17 microns and a readout noise of less than 300 electrons. The interferometer is temperature-controlled to ensure stable performance, and the entire payload has a mass of approximately 5 kg. The FTS payload will be able to provide data on the Martian surface, including wind speed and direction measurements.

Table 12. FTS payload specification.

Characteristics	Value
Mass	5 kg
Power	20 W (peak)
Volume	22.6 × 10 × 17 cm
Scanning	±26° Uni-directional cross track
Pointing	Nadir
Thermal	Deployable Earth shield

FTS CubeSat uses a single STM32-based MCU for its OBDH subsystem, a UHF transceiver for intersatellite link communication, a star tracker for attitude determination, reaction wheels and cold gas thruster for attitude control systems, 6 × 6U and 2 × 3U solar cells approximately generating 50 Wh power in the Mars orbit, which is sufficient for mission accomplishment. Table 13 shows 6U CubeSat with FTS payload mass budget.

Table 13. The 6U CubeSat with FTS payload mass budget and power consumption of subsystems.

Subsystems	Mass (gr)	Size	Power Usage (mW)
MCU (ARM based)	94	9.8 × 9.8 × 1	400
UHF TX/RX	100	9.8 × 9.8 × 1	TX >> 5100 RX >> 240
Antenna	150		
Star tracker	50	3 × 3 × 5	100
Battery and hardware	250	8.9 × 9.5 × 7	500
Solar cells	6 × 300 2 × 150	6U 3U	
Thruster	500	6.4 × 9 × 9	21,000
FTS	5000	22.6 × 10 × 17	20,000
Reaction wheels	520	1U	8000
Structure	1100	6U	0
MLI	200	6U	0
Total	8951		

Figure 14 depicts the computer-aided design (CAD) model and subsystems layout of the Fourier transform spectrometer (FTS) CubeSat. A large amount of the CubeSat's structure is occupied by payload; this property is the same for the other two 6U CubeSats. This research was carried out in our previous paper [71].

The 6U CubeSat with high-quality camera payload: The Chameleon imager is a state-of-the-art hyperspectral instrument designed to deliver imaging capabilities to CubeSats. Its compact design integrates space-qualified control electronics, specialized optics, and a large high-speed data storage system. Table 14 presents the Chameleon imager's technical specifications and Table 15 shows the high-quality CubeSat mass budget. Figure 15 shows the CubeSat structures and subsystem configuration. This product is available on the market [72].

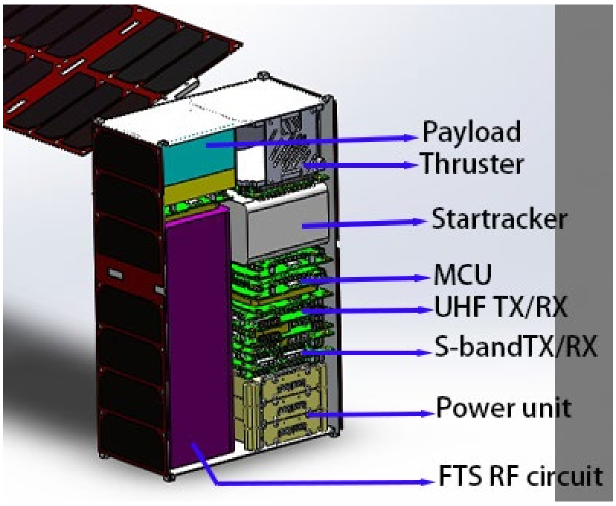

Figure 14. FTS CubeSat subsystem description.

Table 14. High-quality camera (the payload) specification.

Parameters	Value
Spatial resolution (GSD) at 500 km	PAN 10 m; MS 20 m
Swath at 500 km	40 km
Mass (including electronics)	1.6 kg
Spectral bands	7 × MS
Satellite bus size	Compatible with 3U or 6U
Physical size	2U (10 cm × 10 cm × 20 cm excl. electronics) (10 cm × 10 cm × 21.5 cm with rear-mounted CU)
Data interface	LVDS, SPI, I2C, CAN, RS422
Power usage	imaging mode: <10 W; readout mode: <5 W

Table 15. The 6U CubeSat with high-quality camera payload mass budget and power usage.

Subsystems	Mass (gr)	Size	Power Usage (mW)
MCU	94	9.8 × 9.8 × 1	400
UHF TX/RX	100	9.8 × 9.8 × 1	TX >> 5100 RX >> 240
Antenna	150		
Star tracker	50	3 × 3 × 5	100
Battery and hardware	250	1U	500
Solar cells	6 × 300 2 × 150	6U 3U	
Thruster	500	6.4 × 9 × 9	21,000
Camera	1600	2U	10,000
Reaction wheels	520	1U	8000
Structure	1100	6U	0
MLI	200	6U	0
Total	6664		

The 6U CubeSat with HyperScape 100 spectrometer payload: The HyperScape100 spectrometer represents optical payload technology, providing space-based remote sensing capabilities. This device allows for the selection of up to 32 bands within the visible to near-infrared (VNIR) range, with a bandwidth of approximately 3% of the central wavelength. At a 500 km orbital height, it achieves a ground sampling distance (GSD) of 4.75 m. Table 16 provides a detailed overview of the specifications of the HyperScape100 payload, while Figure 16 illustrates the HyperScape 100 spectrometer 6U CubeSat platform. The total mass of this 6U CubeSat is 6664 g, as it utilizes a similar platform to other 6U CubeSats, with the payload mass of 1600 g, the same as the high-quality camera payload. This payload is available on the market [73].

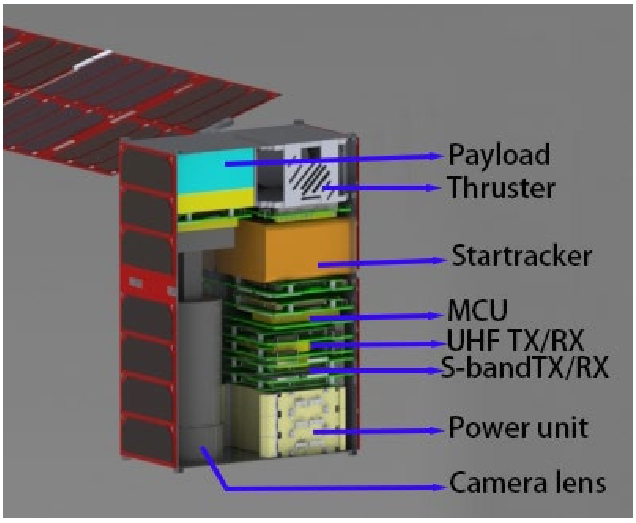

Figure 15. The 6U CubeSat with high-quality camera payload and its subsystems layout.

Table 16. The HyperScape 100 payload parameters.

Parameter	Value
Focal length	580 mm ± 1 mm
Aperture	95 mm
Full field of view	2.22° (across-track)
Sensor technology	CMOS Global Shutter
Resolution	4096 pixels
Pixel size	5.5 µm
Pixel depth	10-bit
Spectral bands	Up to 32 bands user selectable
Spectral range	442 nm to 884 nm
Control interface options	I2 C
Power consumption	2.5 W
Mass	1.1 ± 5%
Dimensions	98 × 98 × 176 mm

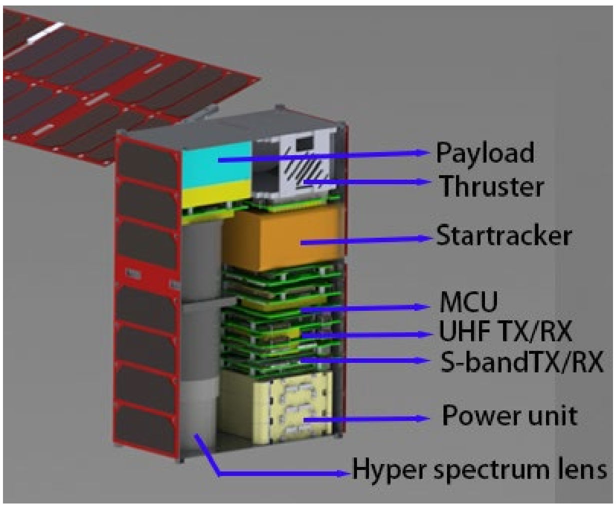

Figure 16. The 6U CubeSat subsystems layouts with HyperScape 100 spectrometer.

The 3U CubeSat with THz payload: We introduce a compact THz radiometer CubeSat standard framework. The THz radiometer's total mass is 1 kg. The payload earns its place the CubeSat for the purpose of studying water vapor absorption in the study of Mars' atmosphere.

To maintain mass equilibrium of the cargo microsatellite, two 3U CubeSats equipped with THz payloads are employed. Table 17 provides the mass budget details for the THz 3U CubeSat. Figure 17 shows THz 3U CubeSat subsystem layouts with the CAD model.

Table 17. THz CubeSat mass budget.

Item	Mass (gr)	Quantity
Thruster	500	1
3U solar cells	150	3
20 Whr battery and hardware	350	1
Main MCU	100	1
UHF transceiver	75	1
UHF ant	50	1
S-band transceiver	132	1
S-band ant	75	2
Star tracker	250	1
Star tracker	250	1
Structure	304	1
THz payload	400	1
Total mass	2761	
Margin	239	

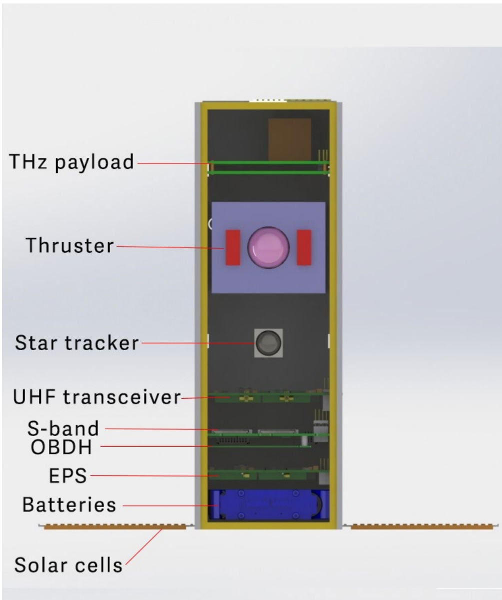

Figure 17. THz 3U CubeSat subsystems layout.

6. The Mission Scientific Payload: Usage of THz Radiometer for Study of Mars Atmosphere

We propose a THz radiometer as a scientific payload for monitoring water vapor in the Martian atmosphere. This approach aids in a deeper understanding of the characteristics of Martian clouds. While there are numerous microwave remote sensing techniques for detecting water vapor particles that are effective, their limitation is that they primarily penetrate and detect large ice particles and cannot discern small water particles. Some studies claim that water vapor particles can be detected by lidar systems. However, these types of instruments are constrained by the satellite's field of view (FOV) [74]. To address these challenges, THz passive remote sensing has garnered significant attention due to its impressive multidisciplinary imaging capabilities [75]. The THz wavelength, with its tiny waveguide, can detect small particles of water within clouds in the atmosphere. Furthermore, THz remote sensing is also sensitive to other types of molecules, such as oxygen, hydrogen, and other vaporous molecules [76]. In the MeSat mission, we propose the THz radiometer payload as a scientific payload. A survey of previous space missions reveals several satellite missions to Mars orbit for atmospheric remote sensing, such as NASA's MAVEN, ExoMars, and the UAE's Hope Probe. It is noteworthy that these satellites are microsatellites, and no papers have reported the use of THz technology for Martian atmospheric investigation with those missions; consequently, to cover the research gap and bring novelty with our THz radiometer, we present the scientific THz payload within two 3U CubeSats and the mothership for remote sensing of the Mars atmosphere to determine water vapor content. It should be noted that the mothership utilizes an active THz radiometer to perform active remote sensing of the Mars atmosphere; therefore, the mothership can collect data day and night; it gives a new objective to the Mars orbiter. Research indicates that THz devices can determine the total thickness and shapes of clouds [77], and previous studies have shown that Mars' atmospheric water vapor averages around 1% [78]. Therefore, we propose the THz radiometer as a scientific mission to scan the Martian atmosphere and give us new, as yet undefined, data from the Martian atmosphere.

To demonstrate that the THz radiometer CubeSat framework is a feasible payload and not a conceptual design, we elaborate on the technical considerations and design aspects of this payload. The other three proposed payloads are commercially available; therefore, we provide a general overview of their properties and discuss the general design of the THz radiometer payload in the next paragraphs.

Complete System Design for THz Spectrometers

In our approach for designing a space THz radiometer, we were inspired by the usage of the THz radiometer within the CubeSat projects RACE [79], MicroMAS-2 [80], TROPICS [81], and MiRaTA [82]. These missions utilize THz signal absorptions of water vapor within the Earth's atmosphere to monitor weather forecasting, cloud formation, and anticipation of tropical cyclones. The overall concept of these missions inspired us to propose a THz radiometer for Martian atmospheric investigation. THz technology can provide accurate views of the Martian atmosphere.

In the past, usage of THz technology was not incorporated with CubeSat, along with several other projects. Additionally, the sensitivity of the THz wavelength to water vapor gives better accuracy, and justifies the first THz payload to Mars. Some existing projects proposed the usage of Schottky diode technology for THz radio frequency conversion for space remote sensing projects [83–106]. A radiometer consists of several key elements for radio signal determination and signal level intensity measurement. Here, we give a general explanation of what engineering layouts suit and support the proposed THz scientific payload. We also explain the usage of sub-harmonic mixer technology for the down conversion of signals. This layout contains a Schottky diode sub-harmonic mixer, a market-available frequency synthesizer, and spectrometer. We show the system's detailed diagrams in Figure 18.

To assess the capability of the proposed scientific THz payload for water detection, an engineering model was tested under controlled lab conditions. This involved using a plastic box filled with two different water levels to observe the amplitude of emitted water signals. Additionally, liquid oil was positioned in front of the radiometer to demonstrate the THz signal's specific effectiveness in distinguishing water. These tests confirm the unique ability of THz signals in identifying water presence and its values. We can see the test results in Figure 19.

In the experiment, the oil yielded signals that were weak, almost negligible. Conversely, the water demonstrated a strong response during frequency sweeps, with signal amplitude increasing proportionally to the volume of water. Specifically, a 24 mL sample of water resulted in a higher output amplitude than a 12 mL sample, indicating a correlation between water volume and signal strength in our measurements.

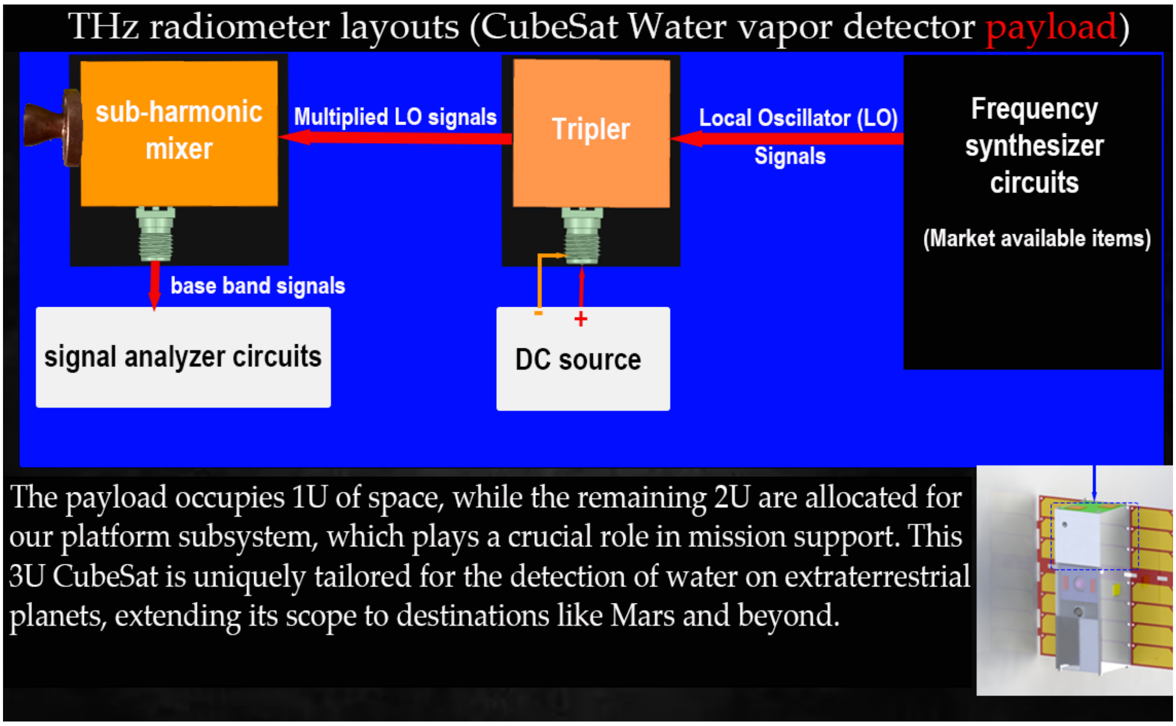

Figure 18. Block diagram of the terahertz (THz) spectrometer.

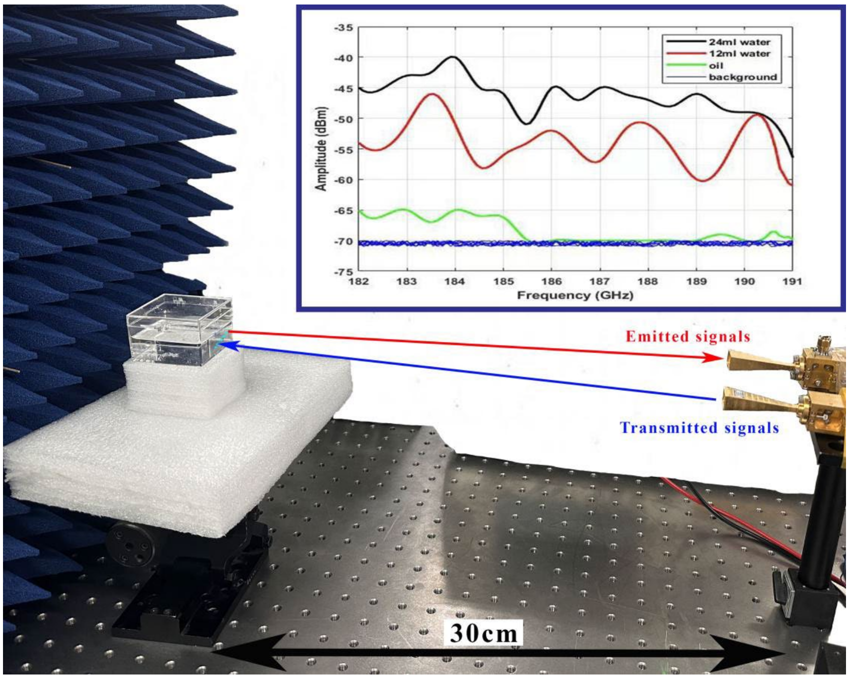

Figure 19. THz radiometer water-detection examination.

7. Expected Data from the Missions

In the proposed MeSat mission, the mother ship employs an active THz radiometer to horizontally analyze the Martian atmosphere water vapor during both day and night in Martian time. Additionally, CubeSats equipped with passive THz radiometers vertically monitor the atmosphere. This dual approach enables the investigation of Martian atmospheric water vapor conditions via THz spectrums. Figure 20 illustrates how MeSat and two 3U CubeSats might operate in Mars' orbit and the expected results.

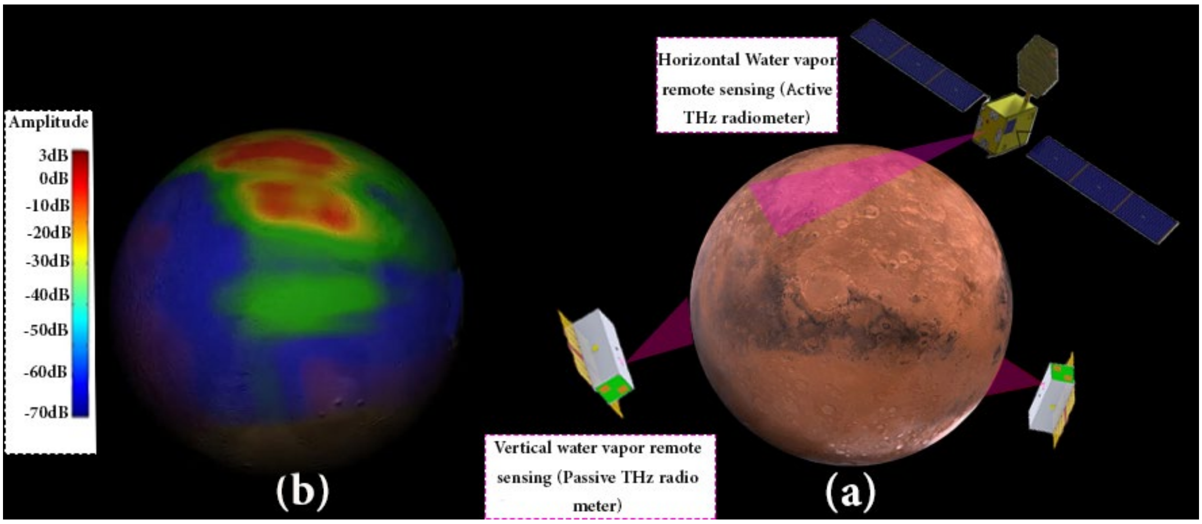

Figure 20. Expected data from THz radiometer payloads. (**a**) CubeSat constellation, (**b**) THz payloads, expected data (the amplitude ranges come from engineering model of THz radiometer; this data can be formulated to atmosphere temperature). Imaginary data from Mars Express mission.

The additional missions will include a spectrometer, camera, and FTS payload, all of which are commercially available. Each payload is designed to enhance the data collected about the Martian environment. These instruments have been chosen to assess Mars' environmental conditions, providing the critical information necessary for fundamental discoveries that support human colonization efforts. Figure 21 shows how the information will be illustrated from three nominated payloads.

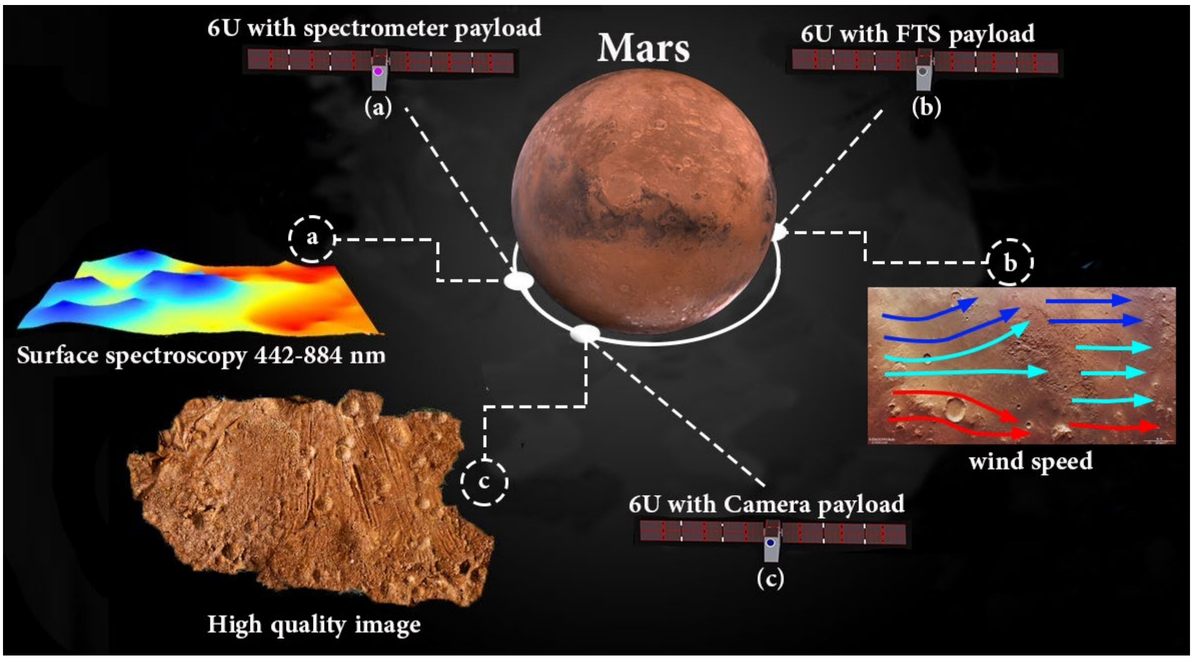

Figure 21. Expected results from 6U CubeSats with FTS, spectrometer, and camera payloads.

8. Conclusions

This paper offers a comprehensive analysis of five proposed satellite systems, meticulously addressing power budgets, mass budgets, and telecommunication considerations.

The mission's diverse payload selection, comprising a 120 kg cargo satellite, specialized CubeSats for photography, imaging spectroscopy, wind speed measurement, and Martian atmospheric investigation, aims to provide environmental research of Mars. The goal of the MeSat project revolves around conducting a comprehensive examination of Mars using a diverse array of payloads. The photography missions are intended to enrich our visual comprehension of Mars, the FTS payloads aim to pinpoint potential habitable zones by scrutinizing environmental cues. Wind speed measurements will offer insights into storm-prone regions or areas suitable for wind-powered electricity generation. The THz radiometer as a scientific payload will give a better insight of Mars' atmosphere, especially its water vapor properties. Each payload contributes unique data crucial to understanding the Martian environment. Another aspect of the MeSat mission showcases the effectiveness of a dual-step hybrid optimization algorithm, the PSO-homotopy. This algorithm efficiently analyzes a fuel-optimized, low-thrust trajectory from Earth to Mars while considering the ephemeris dynamics model, successfully solving the resulting multipoint boundary value problem (MPBVP) with impressive constraint satisfaction. This study also investigates the impact of hyperbolic excess velocity, various Earth launch and Mars rendezvous opportunities, and different types of Hall thrusters and Ion engines. Delivering a payload of 102.8 (kg) to Mars while consuming only 17.2 (kg) of fuel represents a highly efficient and optimized mission. This impressive payload-to-fuel ratio underscores the effectiveness of the trajectory design and propulsion system employed in the mission. Achieving such a high payload mass while minimizing fuel consumption indicates a significant advancement in mission planning and spacecraft propulsion technologies. It showcases the optimization of trajectory maneuvers, propulsion efficiency, and mission design to maximize payload delivery while minimizing the fuel requirement, ultimately enhancing the mission's overall feasibility and cost-effectiveness.

Author Contributions: Methodology, V.R. and M.S.; Investigation, V.R., M.S., K.D.E.K. and M.K.T.; Resources, V.R.; Writing—original draft, V.R.; Writing—review & editing, M.S.; Supervision, W.H.; Funding acquisition, W.H. All authors have read and agreed to the published version of the manuscript.

Funding: This research received no external funding.

Data Availability Statement: Data are contained within the article.

Conflicts of Interest: The authors declare no conflict of interest.

References

1. The Guardian. Available online: https://www.theguardian.com/books/2018/oct/19/brief-answers-to-the-big-questions-stephen-hawking-review (accessed on 19 October 2018).
2. NASA. Available online: https://www.nasa.gov/wp-content/uploads/2015/01/benefits-stemming-from-space-exploration-2013-tagged.pdf (accessed on 20 September 2013).
3. Francesca, F.; Marta, V.P.; Claudia, P. Advantages and Limitations of Current Microgravity Platforms for Space Biology Research. *Appl. Sci.* **2020**, *11*, 68. [CrossRef]
4. The Space Review. Available online: https://www.thespacereview.com/article/3193/1 (accessed on 13 March 2017).
5. Seth, D.B.; Jacob, D.H.; Shawn, D.D. Would contact with extraterrestrials benefit or harm humanity? A scenario analysis. *Acta Astronaut.* **2011**, *68*, 2114–2129. [CrossRef]
6. Sergey, K.; Vladimir, L. Human Life and Evolution in Biospheres on Earth and Outer Space: Problems and Prospects. *Future Hum. Image* **2021**, *15*, 39–58.
7. NASA. Available online: https://www.nasa.gov/image-article/nasas-journey-mars/#:~:text=NASA%20is%20developing%20the%20capabilities,Policy,%20also%20issued%20in%202010 (accessed on 1 December 2014).
8. Alred, J.W.; Siegfried, W.H. Maximization of benefits from the space exploration initiative. *Acta Astronaut.* **1992**, *28*, 357–363. [CrossRef]
9. Bette, S.; Andy, S.; James, B.; Sarah, L.C.; Kevin, S.; Erin, M.; Julie, R. Development of a NASA roadmap for planetary protection to prepare for the first human missions to Mars. *Life Sci. Space Res.* **2023**, *38*, 1–7. [CrossRef]
10. Ritu, S.L. Public-private linkages and the case of asteroid mining. *Technol. Anal. Strateg. Manag.* **2022**. [CrossRef]
11. Matthew, J.H.; Kelly, S.F.; Emily, A.H.; Paul, G.B.; Tim, G.; Cassandra, M.C. Protecting the Planet or Destroying the Universe? Understanding Reactions to Space Mining. *Sustainability* **2022**, *14*, 4119. [CrossRef]

12. Anna, C.S. Challenges and Opportunities for Bioactive Compound and Antibiotic Discovery in Deep Space. *J. Indian Inst. Sci.* **2023**, *103*, 819–832.
13. Harvard International Review. Available online: https://hir.harvard.edu/economics-of-the-stars/ (accessed on 8 April 2022).
14. Pavel, S. Asteroid Mining Tax as a Tool to Keep Peace in Outer Space. *Space Policy* **2023**, *65*, 101555. [CrossRef]
15. Science In The News (SITN). Available online: https://sitn.hms.harvard.edu/flash/2019/water-beyond-earth-the-search-for-the-life-sustaining-liquid/ (accessed on 26 September 2019).
16. Astrobiology at NASA. Available online: https://astrobiology.nasa.gov/education/alp/water-so-important-for-life/#:~:text=It%20is%20abundant%20on%20Earth,the%20planet%20could%20support%20life (accessed on 1 December 2023).
17. Althaf, H.B.; Danish, K. Utilisation of Space Robotics in Making Plans in the Works to Overcome Huge Challenges and Send Humans to Mars By NASA. *TTIRAS* **2022**, *2*, 30–35. [CrossRef]
18. Xiao, S.Y.; Rakhyun, E.K. Twards earth-space governance in a multi-planetary era. *Earth Syst. Gov.* **2023**, *16*, 100173. [CrossRef]
19. NASA Mariner 4 Mission. Available online: https://science.nasa.gov/mission/mariner-4/ (accessed on 5 March 2024).
20. NASA Mars Science. Available online: https://mars.nasa.gov/technology/helicopter/ (accessed on 30 July 2020).
21. Favaloro, N.; Saccone, G.; Piscitelli, F.; Olponi, R.; Leoncini, P.; Catalano, P.; Visingardi, A.; Noviello, M.C. Enabling Technologies for Space Exploration Missions: The CIRA-TEDS Program Roadmap Perspectives. *Aerotec. Missili Spaz.* **2023**, *102*, 187–197. [CrossRef]
22. Liu, X.; Xu, W.; Qi, H.; Ren, X.; Liu, J.; Li, L.; Yan, Z.; Liu, C.; Chen, J.; Zhang, Z.; et al. Development and Testing of the MarSCoDe LIBS Calibration Target in China's Tianwen-1 Mars Mission. *Space Sci. Rev.* **2023**, *219*, 43. [CrossRef]
23. Richard, B. Emirates Mars Mission takes first high-resolution images of Martian moon Deimos. *Phys. World* **2023**, *36*, 11ii. [CrossRef]
24. NASA InSight Mission. Available online: https://mars.nasa.gov/news/9452/nasa-insight-study-finds-mars-is-spinning-faster/?site=insight (accessed on 7 August 2023).
25. Indian Space Agency. Available online: https://www.isro.gov.in/MarsOrbiterMissionSpacecraft.html#:~:text=Mars%20Orbiter%20Mission%20(MOM),,orbit%20on%20Sept%2024,%202021 (accessed on 18 September 2023).
26. NASA. Available online: https://science.nasa.gov/mission/phoenix/ (accessed on 4 August 2007).
27. NASA. Available online: https://science.nasa.gov/mission/mer-opportunity/ (accessed on 7 July 2003).
28. The Planetary Society. Available online: https://www.planetary.org/space-missions/viking (accessed on 5 March 2024).
29. Michael, C.K.; Kenneth, S.E. Mars Global Surveyor Mars Orbiter Camera: Interplanetary cruise through primary mission. *J. Geophys. Res.* **2001**, *106*, 23429–23570. [CrossRef]
30. Saunders, R.S.; Arvidson, R.E.; Badhwar, G.D.; Boynton, W.V.; Christensen, P.R.; Cucinotta, F.A.; Feldman, W.C.; Gibbs, R.G.; Kloss, C., Jr.; Landano, M.R.; et al. 2001 Mars Odyssey Missions Summary. *Space Sci. Rev.* **2004**, *110*, 1–36. [CrossRef]
31. Krasmopolsky, V.A. Vertical distribution of water vapor and mars model lower and middle atmosphere. *Icarus* **1979**, *37*, 182–189. [CrossRef]
32. Seymour, L.H. The vertical distribution of water vapor in the atmosphere of Mars. *Icarus* **1976**, *28*, 269–278. [CrossRef]
33. Michel, D.S. The annual cycle of water vapor on Mars as observed by the Thermal Emission Spectrometer. *J. Geophys. Res.* **2002**, *107*, 25-1–25-19. [CrossRef]
34. McCleese, D.J.; Schofield, J.T.; Taylor, F.W.; Calcutt, S.B.; Foote, M.C.; Kass, D.M.; Leovy, C.B.; Paige, D.A.; Read, P.L.; Zurek, R.W. Mars Climate Sounder: An investigation of thermal and water vapor structure, dust and condensate distributions in the atmosphere, and energy balance of the polar regions. *J. Geophys. Res.* **2007**, *112*. [CrossRef]
35. Luca, M.; Dmitrij, V.T.; Theresse, E.; Riccardo, M.; Francois, F.; Horst, U.K.; Jean, P.B. Annual survey of water vapor behavior from the OMEGA mapping spectrometer onboard Mars Express. *Icraus* **2011**, *213*, 480–495. [CrossRef]
36. Alexander, T.; Anna, F.; Oleg, K.; Frank, M.; Jean, L.B.; Alexander, R.; Michael, D.S. Mars' water vapor mapping by the SPICAM IR spectrometer: Five martian years of observations. *Icarus* **2015**, *251*, 50–64. [CrossRef]
37. Alain, S.J.K.; Michael, D.S.; Scatt, D.G. Understanding the water cycle above the north polar cap on Mars using MRO CRISM retrievals of water vapor. *Icarus* **2019**, *324*, 722–735. [CrossRef]
38. Alexey, A.P. Martian atmospheric water vapor abundances in MY26-30 from Mars Express PFS/LW observations. *Icarus* **2022**, *379*, 114975. [CrossRef]
39. Stevens, M.H.; Cangi, E.M.; Deighan, J.; Jain, S.K.; Chaffin, M.S.; Evans, J.S.; Gupta, S.; Clarke, J.T. MAVEN/IUVS Observations of OH Prompt Emission: Daytime Water Vapor in the Thermosphere of Mars. *JGR Planets* **2024**, *129*, e2023JE007982. [CrossRef]
40. Mikhail, L.; Alexander, T.; Benjamin, T.; Anna, A.F.; Oleg, K.; Kevin, S.O.; Franck, M.; Franck, L. Evidence of rapid hydrogen chloride uptake on water ice in the atmosphere of Mars. *Icarus* **2024**, *411*, 115960. [CrossRef]
41. Alexey, A.P.; Timonthy, H.M.; Michael, D.S. Retrievals of vertical distribution of Martian water vapor from combined day and night MGS TES nadir spectra. *Icarus* **2024**, *409*, 115869. [CrossRef]
42. David, M.S.; Elizabeth, J.S.; Robert, H.G.; Thomas, M.G. Atmospheric absorption of terahertz radiation and water vapor continuum effects. *J. Quant. Spectrosc. Radiat. Transf.* **2013**, *127*, 49–63. [CrossRef]
43. JPL. Mars Exploration Program Analysis Group (MEPAG). Available online: https://mepag.jpl.nasa.gov/reports.cfm (accessed on 30 November 2020).
44. NASA JPL. Available online: https://www.jpl.nasa.gov/missions/mars-exploration-rover-opportunity-mer (accessed on 7 July 2003).

45. NASA. Available online: https://www.nasa.gov/directorates/stmd/6-technologies-nasa-is-advancing-to-send-humans-to-mars/ (accessed on 17 July 2020).
46. Feng, D.; Robin, D.W. Prospects for Water Vapor Detection in the Atmospheres of Temperate and Arid Rocky Exoplanets around M-dwarf Stars. *Astrophys. J. Lett.* **2022**, *925*, L8.
47. Jacob, D. The role of water vapour in the atmosphere. A short overview from a climate modeller's point of view. *Phys. Chem. of Earth Part A Solid Earth Geod.* **2001**, *26*, 523–527. [CrossRef]
48. Adam, J.R.W.S.; Ying, F.; Jonathan, J.F.; Tyler, D.R.; Mark, S.M. Detecting and Characterizing Water Vapor in the Atmospheres of Earth Analogs through Observation of the 0.94 µm Feature in Reflected Light. *Astron. J.* **2020**, *159*, 36.
49. Smithsonian Magazine. Available online: https://www.smithsonianmag.com/science-nature/water-vapor-detected-atmosphere-exoplanet-habitable-zone-180973100/ (accessed on 11 September 2019).
50. Saghamanesh, M.; Taheri, E.; Baoyin, H. Interplanetary Gravity-Assist Fuel-Optimal Trajectory Optimization with Planetary and Solar Radiation Pressure Perturbations. *Celest. Mech. Dyn. Astron.* **2019**, *132*, 1–21. [CrossRef]
51. Saghamanesh, M.; Baoyin, H. Optimal Gravity-Assist Low-Thrust Trajectory Using a Robust Homotopic Approach. In Proceedings of the 2018 IEEE CSAA Guidance, Navigation and Control Conference (CGNCC), Xiamen, China, 10–12 August 2018.
52. George, R.; Srivastava, A.K.; Naidu, P.; Reddy, K.R.; Rao, K.M.M. THz radiometry and imaging—A review. *Infrared Phys. Technol.* **2018**, *87*, 46–64.
53. Sutar, S.S.; Mane, S.R.; Kasar, S.S. Design and Simulation of 557 GHz THz Radiometer for Space Applications. *Procedia Comput. Sci.* **2015**, *70*, 34–39.
54. Knight, S.; Rabideau, G.; Chien, S.; Engelhardt, B.; Sherwood, R. Casper: Space exploration through continuous planning. *IEEE Intell. Syst.* **2001**, *16*, 70–75.
55. Matthew, P.G. The Mars Pathfinder mission. *J. Geophys. Res. Planets* **1997**, *102*, 3953–3965. [CrossRef]
56. NASA. Available online: https://science.nasa.gov/mission/odyssey/ (accessed on 7 April 2001).
57. Arturo, R. Europe's Path to Mars: The European Space Agency's Mars Express Mission. *Hist. Stud. Nat. Sci.* **2011**, *41*, 123–178. [CrossRef]
58. Paul, W.; Michael, D.S. Atmospheric entry profiles from the Mars Exploration Rovers Spirit and Opportunity. *Icarus* **2006**, *185*, 133–142. [CrossRef]
59. Deborah, S.B.; Kevin, P.T. Phoenix surface mission operations processes. *J. Geophys. Res. Planets* **2008**, *113*. [CrossRef]
60. Vandi, V.; Joseph, C.; Stephan, K. The evolution of the curiosity rover sampling chain. *J. Field Robot.* **2019**, *37*, 729–753. [CrossRef]
61. Fowler, C.M.; McFadden, J.; Hanley, K.G.; Mitchel, D.L.; Curry, S.; Jakosky, B. In-Situ Measurements of Ion Density in the Martian Ionosphere: Underlying Structure and Variability Observed by the MAVEN-STATIC Instrument. *JGR Space Phys.* **2022**, *127*, e2022JA030352. [CrossRef]
62. NASA. Available online: https://mars.nasa.gov/mars-exploration/missions/esa-exomars-rover/ (accessed on 12 March 2020).
63. Lange, L.; Forget, F.; Banfield, W.B.; Wolff, M.; Spiga, A.; Millour, E. InSight Pressure Data Recalibration, and Its Application to the Study of Long-Term Pressure Changes on Mars. *JGR Planet* **2022**, *127*, e2022JE007190. [CrossRef]
64. Stefano, C.A. Single-Launch Deployment Strategy for Lunar Constellations. *Appl. Sci.* **2023**, *13*, 5104. [CrossRef]
65. Stefano, S.; Angelo, C.; Alessandra, M.; Erdem, T.; Eric, B.; Bastiaan, B.; Francesco, T. Designing the Radio Link for a Lunar CubeSat: The LUMIO Case. In Proceedings of the 72th International Astronautical Congress (IAC), Dubai, United Arab Emirates, 25–29 October 2021.
66. Terzoli, S.; Abreu, R.; Costa, J.; Rodrigues, H. CubeSat Deep-Space Communication: Link Budget and Modulation Analysis. *Sensors* **2021**, *21*, 4759. [CrossRef]
67. Saghamanesh, M.; Novinzadeh, A. Optimal guidance of spacecraft rendezvous via free initial velocity vector. Proceedings of the Institution of Mechanical Engineers. *J. Aerosp. Eng.* **2014**, *228*, 1020–1032.
68. Saghamanesh, M.; Baoyin, H. A robust homotopic approach for continuous variable low-thrust trajectory optimization. *Adv. Space Res.* **2018**, *62*, 3095–3113. [CrossRef]
69. Saghamanesh, M.; Baoyin, H. Practical Mission Design for Mars Trajectory Optimization Based on the Ephemeris Model and Full Perturbation System. *Adv. Astronaut. Sci.* **2018**, *165*, 1293–1313.
70. Saghamanesh, M.; Taheri, E.; Baoyin, H. Systematic Low-Thrust Trajectory Design to Mars Based on a Full Ephemeris Modelling. *Adv. Space Res.* **2019**, *64*, 2356–2378. [CrossRef]
71. Vahid, R.; Hu, W. Anticipation of Air Pollution Density Patterns Affected by Wind Velocity Based on Fourier Transform Spectrometer Across the Silk Road Countries by Using EcoBeltSat—A 6U CubeSat. *IEEE J. Miniaturization Air Space Syst.* **2021**, *3*, 2–8. [CrossRef]
72. China National Space Administration. Available online: https://www.cnsa.gov.cn/english/n6465652/n6465653/c6809882/content.html (accessed on 23 September 2023).
73. UAE Space Agency. Available online: https://www.emiratesmarsmission.ae/ (accessed on 20 July 2020).
74. eoPortal Satellites Mission Database. Available online: https://www.eoportal.org/satellite-missions/race (accessed on 4 March 2014).
75. Ossenkopf, V.; Menten, K.M.; Güsten, C.; Nyman, L.A. GREAT: The SOFIA high-frequency heterodyne instrument. *Astron. Astrophys.* **2023**, *518*, L1.
76. Nanosat Data Base. Available online: https://www.nanosats.eu/sat/micromas-2 (accessed on 1 January 2018).

77. NASA Portable. Available online: https://weather.ndc.nasa.gov/tropics/ (accessed on 30 June 2021).
78. Vahid, R.; Weidong, H.; Mohammad, K.T. Water Recognition on the Moon by Using THz Heterodyne-Spectrometer for Identifying the Appropriate Locations to Extract Water for Providing Oxygen for Breathing and Fuel for Spaceships' Propulsion on the Moon with CubeSat. *Aerospace* **2021**, *8*, 186. [CrossRef]
79. Biver, N.; Lecacheux, A.; Encrenaz, T.; Lellouch, E.; Baron, P.; Crovisier, J.; Frisk, U.; Hjalmarson, Å.; Olberg, M.; Sandqvist, A.; et al. Wide-band observations of the 557 GHz water line in Mars with Odin. *Astron. Astrophys.-AA* **2005**, *435*, 765–772. [CrossRef]
80. Eliza, S.; Glenn, Z. The Coming the Moon rush: Technology, billionaires, and Geopolitics will all help get us back to the Moon, but they will not be enough to let us live there indefinitely. *IEEE Spectr.* **2019**, *56*, 22–25.
81. Liu, L.; Weng, C.; Li, S.; Husi, L.; Hu, S.; Dong, P. Passive Remote Sensing of Ice Cloud Properties at Terahertz Wavelengths Based on Genetic Algorithm. *MDPI Remote Sens.* **2021**, *13*, 735. [CrossRef]
82. Jingle, L.; Jianming, D.; See, L.C.; Zhang, X.C. Broadband terahertz wave remote sensing using coherent manipulation of fluorescence from asymmetrically ionized gases. *Nat. Photonics* **2010**, *4*, 627–631. [CrossRef]
83. Brown, E.R. Fundamentals of Terrestrial Millimeter-Wave and THz Remote Sensing. *Int. J. High Speed Electron. Syst.* **2003**, *13*, 995–1097. [CrossRef]
84. Jiménez, C.; Buehler, S.A.; Rydberg, B.; Eriksson, P.; Evans, K.F. Performance simulations for a submillimetre-wave satellite instrument to measure cloud ice. *Q. J. R. Meteorol. Soc.* **2007**, *133*, 129–149. [CrossRef]
85. Evans, K.F.; Walter, S.J.; Heymsfield, A.J.; Deeter, M.N. Modeling of Submillimeter Passive Remote Sensing of Cirrus Clouds. *J. Appl. Meteorol.* **1998**, *37*, 184–205. [CrossRef]
86. Evans, K.F.; Stephens, G.L. Microweve Radiative Transfer through Clouds Composed of Realistically Shaped Ice Crystals. Part II. Remote Sensing of Ice Clouds. *J. Atmos. Sci.* **1995**, *52*, 2058–2072. [CrossRef]
87. Buehler, S.A.; Jiménez, C.; Evans, K.F.; Eriksson, P.; Rydberg, B.; Heymsfield, A.J.; Stubenrauch, C.J.; Lohmann, U.; Emde, C.; John, V.O.; et al. A concept for a satellite mission to measure cloud ice water path, ice particle size, and cloud altitude. *Q. J. R. Meteorol. Soc.* **2007**, *133*, 109–128. [CrossRef]
88. Kim, Y.; Reck, T.J.; Nemchick, D.J.; Chattopadhyay, G.; Drouin, B.; Chang, M.-C.F.; Tang, A. A 183-GHz InP/CMOS-Hybrid Heterodyne-Spectrometer for Spaceborne Atmospheric Remote Sensing. *IEEE Trans. Terahertz Sci. Technol.* **2019**, *9*, 313–334. [CrossRef]
89. De Graauw, T.; Helmich, F.P.; Phillips, T.G.; Stutzki, J.; Caux, E.; Whyborn, N.D.; Dieleman, P.; Roelfsema, P.R.; Aarts, H.; Assendorp, R.; et al. The Herschel-heterodyne instrument for the far-infrared. *Astron. Astrophys.* **2010**, *518*, L6. [CrossRef]
90. Mark, B. Mission Design for the Lunar Reconnaissance Orbiter. In Proceedings of the 29th Annual Aas Guidance and Control Conference, Breckenridge, CO, USA, 4–8 February 2006.
91. Weng, C.; Liu, L.; Gao, T.; Hu, S.; Li, S.; Dou, F.; Shang, J. Multi-Channel Regression Inversion Method for Passive Remote Sensing of Ice Water Path in the Terahertz Band. *Atmosphere* **2019**, *10*, 437. [CrossRef]
92. Bradley, R.J. Subharmonic Mixer in CMOS Microwave Integrated Circuit. Ph.D. Thesis, Queen's University, Kingston, ON, Canada, 2009.
93. Zhang, B.; Lv, X.; He, J.; Xing, D.; Fan, Y.; Chen, X. 1.1 THz tenth harmonic mixer based on planar GaAs Schottky diode. *Workshop Millim.-Waves Terahertz Technol.* **2019**, *13*, 1799–1803. [CrossRef]
94. Yang, Y.; Zhang, B.; Zhao, X.; Fan, Y.; Chen, X. 220 GHz wideband integrated receiver front end based on planar Schottky diodes. *Microw. Opt. Technol. Lett.* **2019**, *62*, 2737–2746. [CrossRef]
95. Zhang, B.; Zhang, Y.; Pan, L.; Li, Y.; Cui, J.; Xu, R.; Yan, B. A 560 GHz Sub-harmonic Mixer Using Half-Global Design Method. *Electronic* **2021**, *10*, 234. [CrossRef]
96. Anderberg, M.; Sobis, P.; Drakinskiy, V.; Schleeh, J.; Dejanovic, S.; Emrich, A.; Stake, J. A 183-GHz Schottky Diode Receiver with 4 dB Noise Figure. In Proceedings of the 2019 IEEE MTT-S International Microwave Symposium (IMS), Boston, MA, USA, 2–7 June 2019.
97. Anderberg, M. Design of a 183-GHz Subharmonic Mixer using Membrane Integrated GaAs Schottky Diode Technology. Ph.D. Thesis, Chalmers University of Technology, Gothenburg, Sweden, 2018.
98. Maestrini, A.; Tripon-Canseliet, C. A 540–640-GHz High-Efficiency Four-Anode Frequency Tripler. *IEEE Trans. Microw. Theory Tech.* **2019**, *53*, 2835–2843. [CrossRef]
99. Vahid, R.N.; Weidong, H.; Waseem, S.; Muzahir, A. CubeSat-Based Observations of Lunar Ice Water Using a 183 GHz Horn Antenna: Design and Optimization. *Appl. Sci.* **2023**, *13*, 9364. [CrossRef]
100. Wu, C.; Zhang, Y.; Xu, Y.; Bo, Y.; Xu, R. Dual Lumped Ports Technique and Its Applications in Modeling of Planar Schottky Diode in THz Band. *IEEE Access* **2020**, *9*, 38001–38009. [CrossRef]
101. Guo, J.; Cheng, H.; Xu, J.; Qian, C. Design of a full W-band detector based on Schottky diode with quartez substrate. *IET Microw. Prophage.* **2019**, *13*, 936–941. [CrossRef]
102. Lin, P.; Fang, X.; Zhang, L. Design and Optimization of Half-Waveguide Transitions for Millimeter-Wave Applications. *IEEE Trans. Compon. Packag. Manuf. Technol.* **2019**, *9*, 2209–2216.
103. Ji, G.; Zhang, D.; Meng, J.; Liu, S.; Yao, C. Design and Measurement of a 0.67 THz Biased Sub-Harmonic Mixer. *Electronic* **2020**, *9*, 161. [CrossRef]
104. Liu, Y.; Zhang, B.; Feng, Y.; Lv, X.; Ji, D.; Niu, Z.; Yang, Y.; Zhao, X.; Fan, Y. Development of 340-GHz Transceiver Front end based on GaAs Monolithic Integration Technology for THz Active Imaging Array. *Appl. Sci.* **2020**, *10*, 7924. [CrossRef]

105. Bertrand, T.; Alain, M.; John, W.; Erich, S.; Goutam, C.; John, G.; Choonsup, L.; Robert, L.; Imran, M. Terahertz cooled sub-harmonic schottky mixer for planetary atmospheres. In Proceedings of the 5th ESA Workshop on Millimeter Wave Technology and Application & 31st ESA antenna Workshop, Noordwijk, The Netherlands, 18–20 September 2019.
106. Jose, M.; Perez, E.; Carlos, Q.; Ramon, G.; Inigo, E. Design of 300 GHz combined doubler/subharmonic mixer based on schottky diodes with integrated MMIC based local oscillator. *Electronic* **2020**, *9*, 2112.